

Published in final edited form as:

*J Magn Magn Mater.* 2011 March 1; 323(6): 651–668. doi:10.1016/j.jmmm.2010.09.008.

## The Behaviors of Ferro-Magnetic Nano-Particles In and Around Blood Vessels under Applied Magnetic Fields

A. Nacev<sup>1,4,\*</sup>, C. Beni<sup>2</sup>, O. Bruno<sup>2</sup>, and B. Shapiro<sup>1,3,4</sup>

<sup>1</sup>Fischell Department of Bioengineering

<sup>2</sup>Applied and Computational Mathematics, California Institute of Technology

<sup>3</sup>Institute for Systems Research

<sup>4</sup>University of Maryland at College Park

### Abstract

In magnetic drug delivery, therapeutic magnetizable particles are typically injected into the blood stream and magnets are then used to concentrate them to disease locations. The behavior of such particles *in-vivo* is complex and is governed by blood convection, diffusion (in blood and in tissue), extravasation, and the applied magnetic fields. Using physical first-principles and a sophisticated vessel-membrane-tissue (VMT) numerical solver, we comprehensively analyze in detail the behavior of magnetic particles in blood vessels and surrounding tissue. For any blood vessel (of any size, depth, and blood velocity) and tissue properties, particle size and applied magnetic fields, we consider a Krogh tissue cylinder geometry and solve for the resulting spatial distribution of particles. We find that there are three prototypical behaviors (blood velocity dominated, magnetic force dominated, and boundary-layer formation) and that the type of behavior observed is uniquely determined by three non-dimensional numbers (the magnetic-Richardson number, mass Péclet number, and Renkin reduced diffusion coefficient). Plots and equations are provided to easily read out which behavior is found under which circumstances (Figures 5, 6, 7, and 8). We compare our results to previously published *in-vitro* and *in-vivo* magnetic drug delivery experiments. Not only do we find excellent agreement between our predictions and prior experimental observations, but we are also able to qualitatively and quantitatively explain behavior that was previously not understood.

## 2. Introduction

Magnetic drug targeting refers to the attachment of therapeutics to magnetizable particles, and then applying magnetic fields to concentrate them to disease locations such as to solid tumors, regions of infection, or blood clots [4,8-14]. Though in some cases the magnetizable particles can be introduced into the body outside the blood flow, e.g. as in magnetic treatment of the inner-ear where a small gel containing nano-particles is placed on the round window membrane [19,20], usually ferromagnetic particles are injected into a vein or artery [4-7,9,13,16,21-29]. Particles so injected will circulate throughout the vasculature as the applied magnetic field is used to attempt confinement at target locations. Two main considerations arise from the *in-vivo* use of these particles. First, the particles must be small

\*Corresponding author, alek@umd.edu.

**Publisher's Disclaimer:** This is a PDF file of an unedited manuscript that has been accepted for publication. As a service to our customers we are providing this early version of the manuscript. The manuscript will undergo copyediting, typesetting, and review of the resulting proof before it is published in its final citable form. Please note that during the production process errors may be discovered which could affect the content, and all legal disclaimers that apply to the journal pertain.

enough to make it out from the blood vessels into surrounding tissue (they should be no larger than approximately 400 – 600 nm to extravasate out from even ‘leaky’ tumor vessels [9,25,30-33]), and, more subtly and crucially, they must be small enough to have sufficiently long *in-vivo* residence times (larger particles are removed faster by the mononuclear phagocyte system; in human clinical trials [4,5] Chemicell's 100 nm particles were shown to have 30 min plasma residence times). Second, the magnetic force on these small particles is minimal. Magnetic force scales with particle volume [34], decreasing the size of a particle by a factor of 10 decreases the magnetic force on it by 1000. Even with strong magnetic fields (> 1 Tesla) and high magnetic gradients ( $\approx 0.5$  T/cm), the forces on ferro-magnetic nano-particles remain extremely small, in the range of pico-Newtons [34-36].

Thus a key issue in magnetic drug delivery is whether the applied magnetic forces can compete with convective blood (drag) forces that tend to wash particles away. The questions are: can particles be confined to target regions against blood flow? In which blood vessels and where do they concentrate? How deep within the body can targeting occur? Past animal experiments [6,37-45] and phase I human clinical trials [3,6,7] have observed the accumulation of magnetic nano-particles by visual inspection, magnetic resonance imaging, and histology studies. These have shown that magnetic forces can concentrate micro- and nano-particles *in-vivo* near magnets, but the details of that concentration cannot be seen experimentally. MRI and visual inspection do not have the resolution to show in which vessels magnetic forces have exceeded blood drag forces, and they certainly cannot show where in the vessel accumulation is occurring. Equally, histology studies are carried out after the animal has been sacrificed and blood flow stopped; they speak only partially to where in the blood vessels the particles might have been. Thus, in this paper, we address this issue via simulations. We map the parameter space and characterize what should happen in an idealized blood vessel in terms of applied magnetic force strength and blood flow velocity. Our goal is to forecast and characterize the type of behaviors that will occur.

We note that the usual back-of-the-envelope analysis is not sufficient; it does not predict what is observed experimentally. Consider the rat experiments shown in Figure 1b. Here our collaborators (Lubbe and Bergemann) used a 0.5 Tesla, 5 cm long, 5 mm wide permanent magnet to focus 250 nm diameter iron-oxide nano-particles. Even for a particle at a distance of just 1 mm away from the magnet (just below skin depth), the magnetic force on this particle (see equation (4) and [34, 35]), including the effect of particle magnetic saturation and using an exact solution [46] for the magnetic field around the magnet, is only about  $\approx 1 \times 10^{-13}$  N. By comparison, the Stokes blood drag force [47] on the same particle, for the slowest measured 0.1 mm/s blood-flow velocities in rat capillaries [48-50], is  $\approx 7 \times 10^{-13}$  N, a factor of  $\times 7$  greater. This simple comparison suggests that the field gradient near the magnet cannot capture a 250 nm particle against even the weakest blood flow in a rat. Yet in Figure 1b the dark spots where the particles have been focused can be clearly seen. This focusing was carried out while the rats were alive and their blood was flowing, and it has been repeated even with 100 nm diameter particles where the magnetic forces are  $2.5^3 = 15.625$  times smaller. Clearly, a crude comparison of magnetic forces per particle to Stokes drag is insufficient to match *in-vivo* behavior. This mismatch is also apparent in the literature both for *in-vitro* and *in-vivo* experiments. In *in-vitro* studies (eg. [29, 51]), particles were focused even when centerline stokes drag forces exceeded magnetic forces. In the *in-vivo* cases (eg. [16, 39, 52]), Stokes drag due to the slowest blood flow in the animals/humans exceeded maximum magnetic forces yet particle focusing was still observed.

The rough calculation above is deficient for two main potential reasons. 1) The blood flow drag forces on the particle vary with its position in the blood vessel. A particle at the vessel center-line will experience a higher blood velocity and hence a higher drag force, but a particle near the blood vessel wall will be surrounded by a near zero blood velocity. This

decrease in velocity is due to the flow resistance provided by the vessel wall, the ‘no-slip’ boundary condition [33,53,54]. Thus a particle near the vessel wall will experience a much smaller drag force and can potentially be held by a much smaller magnetic force (see Figure 2, this effect is also noted in [36] for micro-channels). Alternatively 2) the particles might agglomerate to some degree even though they are typically engineered to minimize agglomeration [9,12,25]. This will increase the magnetic force, which grows with volume, much faster than the Stokes drag, which grows with diameter, thus increasing trapping. In this paper we will focus on examining the first issue in detail, as it is the next crucial question. Item 2) is addressed approximately by considering an agglomerated clump as simply a larger ‘super-particle’ (see Section S3.5). Consideration of agglomeration thus folds into our non-dimensional numbers for size and force (discussed in Section 3.2). A more sophisticated, analysis of agglomeration will be carried out in future work.

This paper focuses on systematically characterizing the behaviors of ferromagnetic nanoparticles in a single idealized blood vessel under the action of an applied magnetic force, blood drag, diffusion within the blood, and transport of particles from blood to surrounding tissue (modeled simply as diffusion, as in [31,33]). It includes an ability to predict what happens in shallow and deep, small and large blood vessels, and it resolves the mismatch between experiments and the usual, but simplistic, back-of-the-envelope centerline Stokes drag versus magnetic force calculation described above. It is organized from the simplest scenario to cases that include added features such as spatially varying magnetic forces, blood pulsatility, curved vessel geometry, and skin boundary conditions. These added features do not qualitatively change the three types of nano-particle behaviors observed: blood velocity dominated, magnetic force dominated, and boundary layer formation regimes. In addition, we do not consider cases where the concentration of ferromagnetic nano-particles is sufficiently high to obstruct the flow within a blood vessel. We find that the observed nano-particle concentration behavior in *in-vitro* and *in-vivo* studies is correctly predicted by a single three-parameter non-dimensional map (Figures 5 and 7) that delineates the blood velocity dominated, magnetic force dominated, and boundary layer formation behaviors. Our summary result is simple to use and will enable a more systematic design of future magnetic *in-vivo* drug delivery systems.

Simulating ferrofluid behavior, even in a single straight vessel, is challenging. We created an in-house vessel-tissue-membrane (VMT) numerical solver based on the Alternating Directions Implicit (ADI) method [55-58]. The VMT solver was both more accurate and 500 times faster than COMSOL (a general-purpose commercially available partial differential equation solver often used in the magnetic drug delivery literature, e.g. [51,59]), and it was able to solve cases that COMSOL could not (see Section 3.4.2). Using VMT we were able to solve all cases, though the most challenging cases still took a long time (the case of mass Péclet number equal to  $1 \times 10^8$  in Section 4.3 took 48 hours). There are ways to further improve VMT to make these cases run much faster and this will be reported in future publications as part of our effort to create a general purpose fast and accurate simulation environment for magnetic drug delivery.

The current study is essential to better forecast what happens *in-vivo* in shallow and deep blood vessels under varying circumstances. Our modeling is the next needed major step: it goes beyond a naive back-of-the-envelope calculation but is still tightly focused on the issue of blood convection versus magnetic forces. It necessarily cannot include all the complex details of magnetic particle phenomena *in-vivo*, because much of that behavior is still not well understood at a physiological and physical level and therefore cannot yet be quantified mathematically. For example, extravasation [9,25,31-33,60-62] is an active research field in its own right and the mechanisms that drive it are not yet fully known or characterized. Since extravasation cannot be included in detail at our level of modeling, we represent it

here by a diffusion term (from blood to tissue) that is folded into the effective diffusion coefficient (as is done in [31]). Even with this limitation, our model still provides accurate and effective results that are hard to attain any other way. It is necessary for our larger effort to design controllers that will achieve deep tissue magnetic drug targeting [35,63,64], and its ability to simply but accurately predict *in-vivo* behavior will aid the research efforts of the broader magnetic drug delivery community.

### 3. Simulation of Nano-Particle Behaviors in Blood Vessels

We consider the scenario of a single blood vessel with an inflow of blood and ferro-magnetic nano-particles that are actuated by an externally applied magnetic force. We find that the nano-particles exhibit three distinct and specific behavioral patterns: either velocity dominated (they are washed out of the back of the blood vessel), magnetic force dominated (magnetic forces overcome the blood vessel membrane and surrounding tissue barriers), or they form a boundary layer at the blood/tissue interface. Three non-dimensional numbers are required to determine which behavior is occurring. These three numbers are:

**The Non-Dimensional Magnetic Force Strength (the Magnetic-Richardson Number):**

This number quantifies the ratio between the applied magnetic force and the blood Stokes drag at the vessel centerline. When this number is greater than unity then the magnetic force is larger than the blood Stokes drag force at the vessel centerline.

**The Renkin Reduced Diffusion Coefficient:** This quantifies the ratio between diffusion in the blood vessel membrane and diffusion in the blood. If this number is smaller than unity then particles in the blood vessel membrane diffuse much slower than the same particles in blood.

**The Mass Péclet Number:** This number quantifies the ratio between the maximum centerline blood flow velocity times the average blood vessel width to the total particle diffusion coefficient. When this number is much greater than unity then particle convection occurs much faster than diffusion across the blood vessel width.

#### 3.1. Blood Vessel and Surrounding Tissue: The Idealized Geometry

Figure 2 shows the model geometry: an idealized straight blood vessel contained by an endothelial layer next to an underlying tissue layer. This set-up is a simplified version of the Krogh tissue cylinder [31] and similar to the Krogh cylinder the tissue space is a region between adjacent vessels. The vessel has an inlet at the left-hand side and an outlet at the right-hand side. Blood and a constant concentration of ferro-magnetic nano-particles enter from the left. A magnet is held below the blood vessel and creates a downwards magnetic force.

#### 3.2. Governing Equations

We consider the three main forces acting upon the ferro-magnetic nano-particles. These include blood advection forces induced by blood plasma convection [31,47,65], magnetic drift induced by the applied magnetic field [66-68], and diffusion forces induced both by Brownian diffusion [65] and the scattering effect that colliding and shearing red blood cells have on the nano-particles [69].

##### 3.2.1. Magnetic Forces

**3.2.1.1. Maxwell's Equations for the Magnetic Field:** Electromagnetic fields are classically described by Maxwell's equations [70]. We specialize to the case of magneto-static equations that are appropriate for stationary, or slowly varying, magnetic fields.

$$\nabla \times \vec{H} = \vec{j} \quad (1)$$

$$\nabla \cdot \vec{B} = 0 \quad (2)$$

$$\vec{B} = \mu_o (\vec{H} + \vec{M}) = \mu_o (\vec{H} + \chi \vec{H}) \quad (3)$$

Here  $\vec{B}$  is the magnetic field [T],  $\vec{H}$  is the magnetic intensity [A/m],  $\vec{j}$  is the current density [A/m<sup>2</sup>],  $\vec{M}$  is the material magnetization [A/m],  $\chi$  is the magnetic susceptibility, and  $\mu_o$  is the permeability of a vacuum [ $4\pi \times 10^{-7}$  N/A<sup>2</sup>]. These equations hold true in vacuum and in materials, for permanent magnets (magnetization  $\vec{M} \neq 0$ ), and for electromagnets (current  $\vec{j} \neq 0$ ) [34,67,71]. Through the human body, magnetic fields propagate essentially unchanged because the magnetic susceptibility of tissue is close to zero ( $\chi \approx 10^{-6} - 10^{-4}$  [72,73]). In contrast, the magnetite cores (e.g. Fe<sub>3</sub>O<sub>4</sub>) of ferro-magnetic particles have magnetic susceptibilities 5 to 7 orders of magnitude higher than that of tissue ( $\chi \approx 20$ ), therefore these particles are strongly influenced by magnetic fields [34,67,71].

**3.2.1.2. Magnetic Forces on a Particle:** A single ferro-magnetic particle in a magnetic field will experience a force that depends upon the magnetic field and field gradient around it [63,67,74,75].

$$\vec{F}_M = \frac{4\pi a^3}{3} \frac{\mu_o \chi}{(1+\chi/3)} \left[ \frac{d\vec{H}}{d\vec{x}} \right] \vec{H} = \frac{2\pi a^3}{3} \frac{\mu_o \chi}{(1+\chi/3)} \nabla \left( |\vec{H}|^2 \right). \quad (4)$$

Here  $a$  is the radius of a nano-particle [m] and  $\nabla$  is the gradient operator [with units 1/m]. For simplicity, the hydrodynamic radius is considered to be the same size as the magnetic core radius (the case where they differ is discussed in Section S3.8). The first relation is more familiar and clearly shows that a spatially varying magnetic field ( $d\vec{H}/d\vec{x} \neq 0$ ) is required to create a magnetic force. The second equivalent relation states that the magnetic force on a ferro-magnetic particle is always from low to high magnetic fields and proportional to the gradient of the magnetic field intensity squared. The two relations are equal by the chain rule and it is evident that the magnetic force is also proportional to the particle volume.

If the applied magnetic field is sufficient to saturate the nano-particle, then  $[d\vec{H}/d\vec{x}] \vec{H}$  in equation (4) is modified to  $[d\vec{H}/d\vec{x}] \vec{M}_{sat}$  where  $\vec{M}_{sat}$  is the saturated magnetization of the particle. Since  $\vec{M}_{sat}$  lines up with  $\vec{H}$ , this does not change the direction of the force, only its size. Thus this case is considered within our framework simply by modifying the size of the magnetic force used.

As shown in Figure 3, when the magnet is held at a long distance compared to the blood vessel width, we can assume that the magnetic force is constant in space throughout the blood vessel width and length. This negates the need to solve the magneto-static equations; it is true to within a few percent even for wide blood vessels near magnets, and it does not qualitatively change the resulting nano-particle behaviors (Section S3.3 in Supplementary

Information analyses the case where the magnetic force does vary in space according to the magneto-static equations).

For the rat experiment shown in Figure 1b, the force acting upon a single iron oxide 125 nm radius particle at a 1 mm depth is given by equation (4) to be  $F_M \approx 0.1$  pN. (Here the 0.5 T permanent magnet produces a magnetic field intensity of  $3.7 \times 10^5$  A/m and a magnetic spatial gradient of  $\approx 1 \times 10^7$  A/m<sup>2</sup> at a distance of 1 mm, the particles had a magnetic susceptibility of roughly  $\chi \approx 20$  and saturated at  $\bar{M}_{sat} \approx 448$  kA/m [29].)

**3.2.1.3. Magnetic Forces on a Concentration of Particles (on a Ferrofluid):** A ferrofluid is composed of many magnetizable nano-particles and is essentially super-paramagnetic. Ferrofluids are strongly magnetized in the presence of an external field and then lose their magnetization once the external field is removed due to rapid random particle reorientation [34,67,71]. Neglecting particle-to-particle interactions, which are small due to particle reorientations and anti-agglomeration coatings [9], the magnetic force on each elemental volume of ferrofluid is given by [35,64]

$$\vec{F}_M = \frac{2\pi a^3}{3} \frac{\mu_0 \chi}{(1+\chi/3)} C \nabla \left( \left| \vec{H} \right|^2 \right) \quad (5)$$

where  $C$  is the concentration of the particles [number/m<sup>3</sup>].

**3.2.1.4. Magnetic Drift Velocity: Magnetic Forces versus Stokes Drag:** When the magnetic force of equation (4) is applied to a particle, it will accelerate the particle in the direction of this force until it reaches an equilibrium velocity  $\vec{V}_R$  relative to the surrounding blood (or surrounding tissue). The opposing Stokes drag force on a spherical particle is given by [33, 65]

$$\vec{F}_S = 6\pi a \eta \vec{V}_R \quad (6)$$

where  $\eta$  is the dynamic viscosity of blood [kg m/s]. When the Stokes drag force first equals the applied magnetic force, then the particle has reached its equilibrium relative velocity (magnetic velocity)

$$\vec{V}_R = \frac{a^2}{9\eta} \frac{\mu_0 \chi}{(1+\chi/3)} \nabla \left( \left| \vec{H} \right|^2 \right) = k \nabla \left( \left| \vec{H} \right|^2 \right) \quad (7)$$

where  $k = a^2 \mu_0 \chi / 9\eta(1 + \chi/3)$  is the magnetic drift coefficient. This relative velocity adds to the fluid velocity (equation (8) below) and together they give the net convection plus magnetic drift velocity. (Equation (6) does not include wall effects that modify the drag force on a particle within a few particle diameters of an external obstruction [76, 77]. Equation (7) also does not include magnetic particle-to-particle interaction forces. For an initial discussion of the effects of agglomeration see Section S3.5 in Supplementary Information or [78-80].)

Within the membrane and tissue layers, Stokes drag is not the only limitation to the maximum velocity induced by magnetic forces. There are many obstacles in the form of

cells and extracellular matrix components that inhibit particle movement [31,33,61,81]. These obstacles lead to an analogous magnetic drift coefficient for the membrane and tissue layers. Einstein's relation assumes that these obstacles also inhibit diffusion in a similar manner [31,33]. Therefore the analogous magnetic drift coefficient for the membrane and tissue layer is generated by scaling  $k$  by the Renkin Reduced diffusion coefficient described in Section 3.4.3 [31].

Using the same rat example as before (Figure 1b) and a blood viscosity of 0.003 Pa s, the magnetic drift velocity of the 250 nm diameter iron oxide particles in blood is then  $V_R \approx 1.4 \times 10^{-5}$  m/s, i.e. it is 14  $\mu\text{m/s}$ .

**3.2.2. Advection Forces**—The fluid velocity profile in a channel is curved - it is highest at the centerline and is zero at the walls due to the no-slip boundary condition. For Newtonian fluids in straight channels at steady state, this curved profile is parabolic [65,82]. Blood, however, is a non-Newtonian fluid due to the presence of the clotting protein fibrinogen which causes red blood cells to aggregate at low shear rates. This creates a blunted flow profile known as plug flow [31]. Such a profile can be fit empirically by [83]

$$\vec{V}_B = V_{B\max} \left( 1 - \left( \frac{r}{R} \right)^\zeta \right) \quad (8)$$

where  $\vec{V}_B$  is the velocity in [m/s],  $V_{B\max}$  is the maximum centerline velocity [m/s],  $r$  is the radial location [m],  $R$  is the radius of the vessel [m], and  $\zeta$  is a constant for a particular profile. A value of  $\zeta = 9$  is usually chosen to fit experimental data of the cardiac cycle [83]. This equation removes the need to solve the Navier-Stokes equations for the blood flow profile. In rat vessels the smallest centerline blood velocity is on the order of 0.1 mm/s [48-50], in humans it is 0.5 mm/s [31].

**3.2.3. Diffusion Forces**—There are two main types of particle diffusion that occur within a blood vessel: Brownian thermal motion and particle scattering due to collisions with blood cells.

**3.2.3.1. Brownian Diffusion:** Brownian motion refers to the random motion of particles under the action of thermal fluctuations and is quantified by a diffusion coefficient [31,65]

$$D_B = \frac{k_B T}{6\pi\eta a} \quad (9)$$

that relates the diffusive flux to the concentration gradient of the particles. Here  $k_B$  is the Boltzmann constant and  $T$  is the absolute temperature. For 250 nm diameter particles in blood at body temperature (37°C), the diffusion coefficient is  $D_B \approx 6 \times 10^{-13}$  m<sup>2</sup>/s [25,27,63,67].

**3.2.3.2. Diffusion from Blood Cell Scattering:** Collision of blood cells with nano-particles causes the particles to scatter and can be modeled as additional diffusion [69]. The scattering diffusion coefficient is on the order of  $D_S \approx 10^{-11} - 10^{-10}$  m<sup>2</sup>/s and can therefore be greater than the diffusion due to thermal motion. The total particle diffusion is the sum of thermal and scattering diffusion hence  $D_{Tot} = D_B + D_S$ .

### 3.2.4. Summary of Governing Equations and Boundary Conditions—

The concentration of ferrofluid at each location is a function of time: it increases when the flux of particles to that location is positive and decreases when it is negative [65,76]. The flux is the summation of the three effects discussed above: diffusion, convection by blood flow, and magnetic drift. Thus

$$\frac{\partial}{\partial t} \underbrace{C(x, y, t)}_{\text{FERROFLUID CONCENTRATION}} = -\nabla \cdot \left[ \underbrace{-D_{\text{Tot}} \nabla C}_{\text{DIFFUSION}} + \underbrace{C \vec{V}_B(y)}_{\text{BLOOD CONVECTION}} + \underbrace{Ck \nabla \left( \left| \vec{H}(x, y) \right|^2 \right)}_{\text{MAGNETIC DRIFT}} \right] \quad (10)$$

where  $\vec{V}_B$  is the blood flow velocity. Considering a constant magnetic force acting only in the negative  $y$  - direction and the specific blunted blood flow profile of equation (8), the concentration can then be described by the partial differential equation

$$\dot{C}(x, y) = -\nabla \cdot \left[ -D_{\text{Tot}} \nabla C + C \left( V_{B\text{max}} \left[ 1 - \left( \frac{y}{R} \right)^9 \right], 0 \right) + C(0, -k \nabla H^2) \right] \quad (11)$$

stated in two spatial dimensions, in  $x$  and  $y$ . The concentration inside the tissue is defined more simply by the equation

$$\dot{C}(x, y) = -\nabla \cdot \left[ -D_{T,\text{Tot}} \nabla C + C(0, -k_T \nabla H^2) \right]. \quad (12)$$

Boundary conditions are required to complete the model. At the blood flow inlet, a constant concentration of magnetic particles is imposed (see also Figure 2). At all external boundaries of the tissue-vessel system, the normal diffusive flux is set to zero ( $\hat{n} \cdot D \nabla C = 0$ ) enforcing the requirement that the total flux at those boundaries is exactly the convective flux (so that ferrofluid correctly convects out of the vessel outlet with the blood flow). The interior boundaries between the vessel and endothelial layer, and the endothelial layer and tissue, satisfy two conditions: the ferrofluid concentration is continuous across each interface (no concentration discontinuities), and the ferrofluid that leaves one domain enters another (no ferrofluid is lost or created).

Since in magnetic drug delivery a magnet is often held outside the skin, and nano-particles then concentrate closest to it but do not leave the body, it can be desirable to include a ‘skin’ boundary condition that prevents nano-particles from leaving the tissue (this would be placed at the bottom of the tissue layer in Figure 2). We do not consider this added feature for the majority of the paper because we are interested in ferrofluid behavior in, immediately around, and between blood vessels. Therefore we permit the nano-particles to leave this focused inspection domain. Skin introduces a new complication, the pile-up of nano-particles in the tissue next to it, and it can distort the behavior around blood vessels in a way that depends on tissue thickness. It necessitates a 4<sup>th</sup> non-dimensional number thus requiring a 4-dimensional visualization of the prototypical behavior of ferro-fluids. A skin boundary condition is included in Section S3.6 in Supplementary Information and correctly causes ferrofluid to pile-up near the magnet.



### 3.3. Range of Physical Parameters

**3.3.1. Magnetic Parameters**—Magnetic nano-particles are usually defined as a moiety between 1 nm and 1  $\mu\text{m}$  that contain a magnetic core [9]. The magnetic core is usually composed of magnetite or maghemite [4,9,21,27,29,51,84-86] but other exotic materials can be used including cementite [45,87]. For *in-vivo* studies the size of particles used ranges from  $\approx 10$  nm (small carriers) [27] to 5  $\mu\text{m}$  (large carriers) [45,87]. Smaller particles (size  $< 25$  nm) usually exhibit superparamagnetic behavior that helps reduce agglomeration when the magnetic fields are removed [9]. Larger particles (size  $> 60$  nm) benefit from not passing through normal fenestrated capillaries where the pore cut-off size is approximately 60 nm [9,25].

The magnetic fields generated by external magnets in *in-vitro* studies have ranged anywhere from  $\approx 70$  mT [8] to  $\leq 1.5$  T [10,51]. Animal trials have had ranges between 0.1 T and 1.5 T [6,21,27,28,39]. While the FDA has approved magnetic strengths up to 8 T for use with humans [9] and human clinical trials have utilized 0.2 to 0.8 T magnet field strengths [4-7]. Most often permanent magnets have been used with sizes ranging from tens of millimeters to tens of centimeters [4,8,21,45,51,87]. Occasionally electromagnets were utilized [10,85]. The distance of particles from magnets has ranged from  $\approx 1$  mm to  $\approx 12$  cm in the literature [7,29,39,87], but we consider up to 30 cm distances to examine the possibility of deep tissue magnetic targeting [35,63,64].

**3.3.2. Advection Parameters**—In humans, typical centerline blood velocities range from 0.5 mm/s in capillaries to the largest value of 40 cm/s in the aorta [31,33,69]. Average vessel diameters vary between 7  $\mu\text{m}$  for capillaries to 3 cm in the vena cava [9,31,69].

**3.3.3. Diffusion Parameters**—Particle size and vessel radii impact the diffusion of nano-particles. The largest diffusion coefficients occur in large vessels (arterioles and arteries) where cell scattering effects are high and with small particles where Brownian diffusion is large. The smallest diffusion coefficients occur in small vessels (capillaries) where scattering effect are negligible and with large particles where Brownian diffusion is small. The typical range in humans of total particle diffusion coefficients is between  $1 \times 10^{-14}$  to  $6 \times 10^{-10}$   $\text{m}^2/\text{s}$  [31,69].

### 3.4. Non-Dimensional Governing Equations: The 3 Key Numbers

Non-dimensionalization of the mathematical model is crucial for mapping out ferrofluid behaviors; it reduces the number of parameters from the 16 in Table 1 to three key independent numbers and it prevents repeatedly solving self-similar cases that have differing dimensional parameters but share the same behavior [76]. Non-dimensional numbers achieve this saving by capturing the ratios between competing physical effects thus illustrating which effects win when and by how much.

We non-dimensionalize equation (10) by choosing a characteristic length scale (the width of the blood vessel  $d_B$ ), a characteristic velocity (the maximum centerline velocity in the blood vessel  $V_{B \text{ max}}$ ), and a characteristic concentration (the nano-particle concentration at the blood vessel inlet  $C_o$ ), and then normalize each variable with respect to these three characteristic quantities. Section S1 in Supplementary Information defines all the resulting non-dimensional variables and provides a detailed derivation of the final equations. After non-dimensionalization, equation (10) becomes

$$\frac{\partial C_B}{\partial t} = -\nabla \cdot \left[ -\frac{1}{Pe} \nabla C_B + (\vec{V}_B + (0, -\Psi)) C_B \right] \quad (13)$$

now where  $C_B$  is the non-dimensional concentration of nano-particles in the blood and  $\vec{V}_B$  is the non-dimensional blood velocity. Equations (14) and (15) are the non-dimensional analogs for transport of magnetic particles in the endothelial membrane and in tissue respectively

$$\frac{\partial C_M}{\partial t} = -\nabla \cdot \mathbf{D} \left[ -\frac{1}{Pe} \nabla C_M + (0, -\Psi) C_M \right] \quad (14)$$

$$\frac{\partial C_T}{\partial t} = -\nabla \cdot \mathbf{D}_T \left[ -\frac{1}{Pe} \nabla C_T + (0, -\Psi) C_T \right]. \quad (15)$$

This normalized model is completely parameterized by 4 non-dimensional numbers: the magnetic-Richardson number  $\Psi$ , the mass Péclet number  $Pe$ , the Renkin reduced diffusion coefficient  $\varphi$  for endothelial membrane diffusivity compared to blood, and the Renkin reduced diffusion coefficient  $\varphi_T$  for the diffusivity of tissue compared to that of blood. The thin endothelial membrane either effectively acts as a barrier to nano-particles or not, thus it suffices to vary either  $\varphi$  (when the membrane limits transport) or  $\varphi_T$  (if tissue limits transport). Since there is little need to vary both, 3 non-dimensional numbers are sufficient to completely characterize nano-particle behavior.

**3.4.1. Magnetic-Richardson Number**—Based on the Richardson number [65,88], we define a magnetic-Richardson number as the ratio of the magnetic force to the Stokes drag force that would act upon a single stationary particle at the centerline of a blood vessel. The magnetic-Richardson number is thus the ratio

$$\Psi = \frac{\text{Magnetic Force at Centerline}}{\text{Stokes Drag Force at Centerline}} = \frac{\left| \frac{\vec{F}_M}{\vec{F}_S} \right|}{\left| \frac{\vec{F}_M}{\vec{F}_S} \right|} = \frac{6\pi a\eta k \nabla \left( \left| \vec{H} \right|^2 \right)}{6\pi a\eta V_{Bmax}} = \frac{\vec{V}_R}{V_{Bmax}} \quad (16)$$

As the magnetic-Richardson number increases to a value greater than unity, the magnetic forces experienced by a particle are much higher than the drag forces created by the blood velocity. As the number decreases below unity, the blood velocity forces dominate.

For the smallest rat blood vessels, the magnetic force upon an iron oxide 250 nm diameter particle at 1 mm depth was 0.1 pN. The Stokes drag force on that same particle in a rat blood vessel with a centerline velocity of 0.1 mm/s is 0.7 pN. Therefore the magnetic-Richardson number in this case is  $\Psi = 0.14$ .

**3.4.2. Mass Péclet Number**—Here the mass Péclet number [31,65,82] is defined as the ratio of the blood vessel width multiplied by the maximum centerline blood velocity to the total diffusion coefficient of the nano-particles within the vessel. At large Péclet values, the blood advection of nano-particles far exceeds their diffusion.

$$Pe = \frac{\text{Blood Vessel Width} \times \text{Maximum Blood Velocity}}{\text{Total Diffusion Coefficient of Particles}} = \frac{d_B V_{Bmax}}{D_{Tot}} \quad (17)$$

Continuing with our rat example, with a centerline velocity of 0.1 mm/s (the slowest measured in a rat capillary), a vessel diameter of  $d_B \approx 6 \mu\text{m}$ , and a nano-particle in blood diffusion coefficient of  $D_{Tot} \approx 6 \times 10^{-13} \text{ m}^2/\text{s}$ , the mass Péclet number is  $Pe \approx 1000$ .

**3.4.3. The Renkin Reduced Diffusion Coefficient**—The behavior of semi-permeable membranes, such as the blood vessel wall, can be modeled by the Renkin reduced diffusion coefficient [31,33]. This coefficient is the ratio of the diffusion coefficient in the membrane to the diffusion coefficient in the blood.

$$D = \frac{\text{Diffusion Coefficient in Membrane}}{\text{Total Diffusion Coefficient in Blood}} = \frac{D_M}{D_B + D_S} = \frac{D_M}{D_{Tot}} \quad (18)$$

As this ratio decreases towards zero, the ferrofluid increasingly remains within the blood vessel. As the ratio increases towards unity, the ferrofluid begins to leave the vessel and enters the membrane. When this ratio is one, the ferrofluid behaves as if the vessel wall did not exist. With this number the permeability of the endothelial membrane can be varied in a simple manner.

If pore diameters of a membrane are known, the following equations can be used to estimate the ratio of blood to tissue diffusion coefficients

$$\frac{D_M}{D_B} = (1 - \alpha)^2 (1 - 2.1044\alpha + 2.089\alpha^3 - 0.948\alpha^5), \alpha = \frac{a}{r_{pore}} \quad (19)$$

where  $r_{pore}$  is the average radius of the pores in a membrane [31,33,89]. For normal endothelial pores of size  $r_{pore} \approx 60 \text{ nm}$  in rat capillaries [48-50],  $\alpha \approx 0$ , while in leaky blood vessels where  $r_{pore} \approx 600 \text{ nm}$ ,  $\alpha \approx 0.36$ .

Not only is the ratio of membrane to blood diffusion coefficients important, but the ratio of tissue to blood diffusion coefficients impacts particle behavior. Similar to the semi-permeable vessel wall, tissue diffusivity is highly dependent upon particle size and the extra-cellular spacing. Therefore it is necessary to vary this number as well, and this is accomplished in Section S3.7.

$$D_T = \frac{\text{Diffusion Coefficient in Tissue}}{\text{Total Diffusion Coefficient in Blood}} = \frac{D_T}{D_{Tot}} \quad (20)$$

Tissue diffusivity is usually greater than the membrane diffusivity but is typically less than the total blood diffusivity. In the rat example, for a tumor extracellular space of  $1 \mu\text{m}$ ,  $\alpha_T \approx 0.56$  [31].

### 3.5. Numerical Implementation

Magnetic particle behavior was simulated by using both the commercial multi-physics package COMSOL ([www.comsol.com](http://www.comsol.com)) and by an algorithm designed specially to meet the significant challenges posed by the Vessel-Membrane-Tissue (VMT) convection diffusion problem. The second method is based on a combination of: 1) a graded mesh to adequately resolve thin boundary layers; 2) the Alternating Directions Implicit (ADI) method [58]; 3) an on-and-off fluid-freezing methodology that allows for efficient treatment of the multiple-time scales that exist in the problem; and 4) a change of unknowns that enables evaluation of steady states in tissue and membrane layers through a highly accelerated time-stepping procedure [55-58]. The resulting linear-time unconditionally-stable numerical methodology, called the VMT solver, is both significantly more accurate and up to four orders of magnitude faster than the COMSOL simulation, in addition to being capable of resolving thin boundary layers for cases where COMSOL fails. For example, considering the case of  $Pe = 1000$ ,  $\Psi = 0.0001$ ,  $\phi = 0.01$ ,  $\phi_r = 0.1$ , on a Intel Xenon quad core 3.1 GHz processor with 80 GB of available memory, COMSOL obtained a solution within 48 hours while our VMT solver obtained a steady state solution with 5 digits of accuracy in only 5 minutes and using 32.7 MB of memory. For another, much more difficult case using  $Pe = 10000$ ,  $\Psi = 0.00001$ ,  $\phi = 0.001$ ,  $\phi_r = 0.01$ , our VMT solver obtained a steady state solution with 5 digits of accuracy in under 8 minutes and using just 98.3 MB of memory while COMSOL was unable to provide a solution.

Full details of the numerical methodology (with additional accuracy and computing improvements resulting from use of the novel Fourier Continuation-Alternating Directions method [90]) used in the VMT solver will be presented in a forthcoming contribution [91].

## 4. Simulation Results

### 4.1. Mapping the Three-Parameter Space

Each simulation of equations (13) to (15) calculated the time sequence and ending equilibrium concentration of ferromagnetic nano-particles as a function of location in blood and tissue. From this concentration data, cross-sectional plots spanning the diameter of the tissue-vessel system were generated. By varying the three non-dimensional numbers, three distinct particle behaviors were observed. These behaviors were then delineated on a plot of Renkin reduced diffusion coefficient versus magnetic-Richardson number for a given mass Péclet number (Figure 5). Péclet number dependence is subsequently shown in Figure 7.

### 4.2. The Three Prototypical Behaviors

The three prototypical behaviors are shown below with an early, intermediate and steady state time snapshot.

**4.2.1. Magnetic Force Dominated Behavior**—In this regime the applied magnetic forces dictate particle behavior. Here the magnetic forces control the transport of the particles irrespective of the blood drag forces. It turns out that when the magnetic force is dominant and is constant, the equilibrium concentration will approach a constant value throughout the tissue-vessel system being considered. The constant downward magnetic force pulls the nano-particles from the blood vessel inlet downwards into the tissue and out the bottom, and any transient concentration gradients are smoothed out by diffusion. Here the maximum concentration never exceeds the inlet concentration, as shown in Figure 4(A). This is a reasonable result since we are assuming the blood vessel sees a constantly replenished supply of nano-particles (from the rest of the body). The applied (approximately constant) magnetic force and diffusion then serve to distribute that concentration of nano-particles equally throughout the region of tissue below the blood vessel and above the

magnet. Here the applied magnetic field does not concentrate particle concentration in the blood vessel or surrounding tissue.

**4.2.2. Velocity Dominated Behavior**—In velocity or Stokes drag dominated behavior the blood drag force on a stationary particle far exceeds the magnetic and diffusion forces. Here the blood velocity washes the particles out the back of the vessel before magnetic forces have had a chance to affect them, as shown in Figure 4(B). Since the inlet of the vessel is always refreshing the fluid flow with the inlet concentration, the overall concentration in the blood remains near that of the inlet concentration. Particle concentration in the tissue is much lower even for long times but eventually, by diffusion, reaches a steady state where the concentration in the tissue is equal to that in the blood vessel. This case acts as if there is no magnet at all since blood forces far exceed its effect. Due to the speed of each effect, different time scales for the ‘early’ and ‘middle’ frames were chosen in Figure 4 so that the middle panels could illustrate the intermediate concentrations of each behavior.

**4.2.3. Boundary Layer Formation**—The boundary layer regime occurs when the magnetic and blood drag forces are comparable; it is the most interesting case. Figure 4(C) illustrates this case. In this regime, the nano-particles build-up near the vessel wall, either inside the vessel where the blood velocity is near zero and/or in the membrane next to the vessel build-up (by diffusion). The concentration elsewhere in the blood essentially remains at the set inlet concentration. In this case the concentration of nano-particles near the vessel wall can exceed the inlet concentration by double or higher. Compared to the previous velocity dominated behavior, which also exhibits a slight build-up of particles along the vessel wall, we define the ferrofluid behavior as forming a boundary layer when

$$C_{B,vessel-wall} \geq 1.01 C_{B,inlet}. \quad (21)$$

In addition, it is this case which has the potential to increase the nano-particle concentration within the tissue to above the unit (blood inlet) concentration, Figure 4(C(ii)). It is this boundary layer regime that illustrates how a focusing of nano-particles is possible even if the magnetic force is substantially smaller than the centerline drag force (as in the rat example of Figure 1b).

### 4.3. Summary of Behaviors under Non-dimensional Number Variations

For ferro-magnetic nano-particles under the action of diffusion, blood convection, and a magnetic force in a straight idealized blood vessel surrounded by tissue, we find three behavior regimes: magnetic dominated, blood velocity dominated, and a boundary layer formation regime. Only in the boundary layer case is the ferrofluid concentrated by the applied magnetic field (Figure 4(C)). In the magnetic and velocity dominated cases it escapes, either out the bottom of the tissue or through the blood vessel outlet. In these two cases it is only the constant re-supply of ferrofluid at the vessel inlet that provides the steady state ferrofluid concentrations shown in Figure 4(A and B).

For the simulation results below, the behavior of any case is grouped into one of these 3 regimes by analyzing the equilibrium concentration profile across the vessel cross-section. If the steady state cross-sectional concentration is uniformly equal to the inlet concentration then the behavior is classed as magnetic dominated; if the steady state vessel wall concentration build-up is less than + 1% of the inlet concentration then it is classed as velocity dominated; and if the cross-sectional concentration exhibits high vessel wall concentration build-up then it is classed as boundary layer formation. In all cases, this

classification exactly matches the qualitative classification based on transient and equilibrium behavior shown in Figure 4.

According to the range of dimensional parameters given in Table 1, the three key non-dimensional numbers were correspondingly varied between  $10^{-8}$  and 30 for the magnetic-Richardson number, between  $10^{-4}$  and 1 for the Renkin reduced diffusion coefficient, and between 30 and  $1 \times 10^8$  for the mass Péclet number. To examine the behaviors at a constant mass Péclet number, simulations were conducted over a logarithmically-spaced grid of 7 magnetic-Richardson and 5 Renkin numbers. Then, to determine the dependence on the Péclet number, the Péclet number was varied over 7 values while the Renkin number was held constant and the Richardson number was varied. This provided a general understanding of the non-dimensional number space. To precisely identify the locations of delineations between the 3 behavioral domains, simulations were completed over two fine grids. First, a fine grid of 10 magnetic-Richardson, 1 Renkin, and 9 Péclet numbers was used. Then, a grid of 13 Renkin, 6 magnetic-Richardson, and 7 Péclet numbers was used. In total, this yielded 720 cases that were simulated and analyzed. Figure 5 and 7 below summarize the results and show the behavior delineations. Then random cases were simulated to verify the defined delineation regions.

Figure 5 illustrates the behavior trends at a mass Péclet number of 333 (i.e. the convection of the nano-particles is 333 times faster than their diffusion through the blood vessel width). It shows the regions in which the three behavior types occur. The velocity dominated region occurs at low magnetic-Richardson numbers where the Stokes drag forces are much larger than the magnetic forces. Meaning, there is a cutoff value at which the Stokes drag forces are able to overcome the magnetic forces sufficiently so that concentration build-up within the vessel is negligible. In contrast, at moderate and higher magnetic-Richardson numbers, the Stokes drag forces are not as effective and a highly concentrated boundary layer develops. However, as the Renkin reduced diffusion coefficient is increased, this ferrofluid boundary layer region occurs less readily, because any build-up of particle concentration in the endothelium can more easily diffuse out into the vessel and be swept away by blood convection. Thus the velocity dominated behavior will also occur in circumstances where the membrane provides a weaker barrier to particle movement described by a larger Renkin reduced diffusion coefficient. This is shown by the curving gray line in Figure 5. But, at near unity Renkin reduced diffusion coefficients, the diffusion coefficients in the blood, endothelial membrane, and tissue are approximately the same and the particles see no difference between these three media leading to magnetically dominated behavior where magnetic forces pull particles downwards through the membrane and tissue towards the magnet.

Figure 6 illustrates the shift in behavior regimes with changing mass Péclet number. The changing Péclet number moves the behavior regimes on the magnetic-Richardson and Renkin axes. As the mass Péclet number decreases, i.e. as particle diffusion increases compared to their convection, the boundary between the velocity dominated and the boundary layer region shifts towards larger magnetic-Richardson numbers where larger magnetic forces are required to overcome the Stokes drag forces. As the particles are able to move more freely due to higher diffusion effects, they do not easily concentrate within the vessel and require larger magnetic forces to retain them near the vessel wall. In addition, it can be seen that at low mass Péclet numbers ( $< 50$ ), the magnetic dominated region begins to grow in size and stretch to lower Renkin reduced diffusion coefficients.

The shift in the velocity-dominated/boundary formation behavior delineation,  $\lambda$ , due to a mass Péclet number change can be approximated by a power law fit  $\lambda \approx 0.0032 Pe^{-0.6} - 1.3 \times 10^{-7}$  that has an  $R^2$  value of 0.99998 (Figure 7). As the mass Péclet number

increases, the delineation shifts to smaller magnetic-Richardson numbers. At a mass Péclet number of  $Pe > 2.1 \times 10^7$ ,  $\lambda = 0$  and the characteristic behavior will be boundary layer formation. This suggests that at very large mass Péclet numbers (at very high blood velocities in big vessels) the nano-particles will build-up along the blood vessel even with very small applied magnetic forces. This is because we assume that the particles continue to be supplied at a constant concentration at the inlet of the blood vessel (Figure 2) from the rest of the body. As they flow quickly to the right, the downward magnetic force brings them to the blood vessel wall predicting a sharp boundary layer due to the now, in comparison, small effect of diffusion. In practice when there are very large blood velocities, only few nano-particles immediately near the blood vessel wall will be captured during the short time that the nano-particles remain within the vessel before they flow out the back. This leads to a very thin boundary layer formation of only a few particles at high mass Péclet numbers.

Figure 8 can be used to determine the blood vessel concentration ( $C_{B,vessel-wall}$ ) for a given magnetic-Richardson number and mass Péclet number. The blue curves correspond to constant mass Péclet numbers and illustrate the blood vessel wall concentration's dependence upon magnetic-Richardson number. The concentration cutoff requirement of  $> +1\%$  (equation (21)) is depicted by a red line, while an alternate equally-valid cutoff requirement of  $> +10\%$  is depicted by a dotted orange line. While equation (21) was used to define the behavior boundary delineation, a larger blood vessel wall concentration could easily be chosen and determined by Figure 8.

Figures 5, 6, 7, and 8 can be used to quickly look up the expected behavior of any magnetic drug focusing experiment. For an *in-vivo* setting, from a knowledge or expectation of the experimental parameters, the magnetic field strength, the magnetic field gradient, particle size, considered blood vessel depth, width, blood centerline velocity, and membrane pore size, the designer should compute or estimate the magnetic-Richardson number (equation (16)), the Renkin reduced diffusion coefficient (use the smaller of the two Renkin numbers between the endothelial membrane (18), (19) and the tissue (20)), and the Péclet number (equation (17)). Then look up the resulting expected behavior in Figure 5 or Figure 6. (Use the  $\lambda$  fit equation of Figure 7 to find the location of the boundary between the velocity and boundary layer formation cases if your Péclet number is not one of those shown in Figure 6.)

The analysis above predicts experimental results in the literature extremely well, for both *in-vitro* and *in-vivo* cases (see the next section). However, it still treats an idealized case. Additional model features, such as pulsatile blood flow, curved blood vessels, particle agglomeration, and skin boundary conditions are included in Supplementary Information Section S3. Except for the effect of skin, which can significantly distort the ferrofluid concentration profile for blood vessels very near it, we find that none of these effects make a substantial difference – the behavior is still magnetic dominated, velocity dominated, or forms a boundary layer essentially as outlined in Figure 5 and 7.

## 5. Comparison with Experiments

Several experimental studies currently published ranging from *in-vitro* glass vessels to *in-vivo* animal targeting have been studied and compared to our predicted behavior. Each experiment can be compared against Figures 5, 6, 7, and 8. We find excellent agreement between prior published experimental observations and our predictions – in fact, there are multiple cases where we can now explain behavior that was not previously understood.

### 5.1. Analyzing Ferrofluid Transport for Magnetic Drug Targeting [51]

Ganguly *et al.* attempted to capture ferrofluid particles within a glass tube containing a moving fluid by using a permanent magnet located beneath the tube. The set-up is analogous to the one presented in this paper allowing for an easy comparison. Table 2 shows the parameters used in this experiment and the corresponding values of our three non-dimensional numbers.

It is important to note that in this experiment, the particles are injected into the bottom  $1/16^{\text{th}}$  section of the glass pipe. They continue axially along this radial location until they encounter the magnet. Therefore although the maximum velocity of the fluid within the pipe is 2.5 cm/s, the maximum fluid velocity experienced by the particles is 4.8 mm/s (assuming a parabolic velocity profile). This produces the  $\Psi$ ,  $Pe$ , and  $\phi$  non-dimensional numbers noted in the ‘Ganguly’ column of Table 2.

Here the Renkin reduced diffusion coefficient is not applicable because there is only a single vessel domain. Thus the behavior of the particle concentration is dependent solely upon the magnetic-Richardson and mass Péclet numbers. The mass Péclet number leads to the estimation of the velocity/ boundary layer delineation position  $\lambda$ . By comparing this value to the magnetic-Richardson number, the behavior type can be determined. Since  $\Psi = 9 \times 10^{-5} \gg \lambda = 1.6 \times 10^{-6}$  this places the predicted behavior squarely within the boundary layer formation regime (even though the centerline Stokes drag far exceeds the maximal applied magnetic force,  $\Psi \ll 1$ ). We thus correctly predict the experimentally observed boundary-layer formation region where the usual Stokes drag vs. magnetic forces back-of-the-envelope analysis fails.

### 5.2. Site-directed Research of Magnetic Nano-particles in Magnetic Drug Targeting [29]

Similar to the experiment described above, Xu *et al.* captured moving nano-particles within a glass tube using a permanent magnet. Xu's experiment, in contrast to Ganguly, includes a magnet located farther away and a spherical capturing chamber is used (the glass tube spreads out into a spherical bulb and then goes back to a straight tube). The bulk fluid velocity was adjusted, and the retention percentage within the capturing chamber was quantified for various speeds. The authors noted that the retention was 100% at a 5.3 mm/s and  $\approx 15\%$  at 100 mm/s. The parameter values for these cases are shown in Table 2 under ‘Xu’.

Similar to Ganguly's experiment, due to a single vessel domain the Renkin reduced diffusion coefficient is not applicable. As above, the delineating boundary position  $\lambda$  and the magnetic-Richardson number  $\Psi$  are compared for the two cases Xu *et al.* considered. When the fluid velocity is 5.3 mm/s, the magnetic-Richardson number is  $\times 25$  larger than the behavior delineation  $\lambda$ . This comparison implies behavior well within the boundary layer regime. However, to correlate this behavior to the measured capture percentage requires determination of the boundary thickness that develops before the capture region. Since nano-particles were not pre-mixed with the fluid but instead injected into the flow, the particles retain their initial injection position within the flow section. If the particles are assumed to be in the lower quarter of the flow near the magnet (a reasonable assumption if the particles were injected with minimal velocity), then the boundary layer that is swept into the spherical capturing chamber can be determined. If the particles are flowing at 5.3 mm/s then the capture percentage predicted by a simulation of this case was  $\approx 100\%$  which matches the measured 100% retention by Xu *et al.* When Xu set their velocity to the higher 100 mm/s value, only 15% of the particles were captured in their experiment. In this case the delineating boundary position  $\lambda$  is a little closer to the magnetic-Richardson number ( $\lambda$  is  $\times$



18 greater than  $\Psi$ ). The percentage captured predicted by a simulation of this case was 13% which closely matches the 15% retention measured by Xu *et al.*

Xu *et al.* commented that the standard force comparison (capture force requirements versus magnetic forces) did not predict the occurrence of their observed behavior. They suggested that the particles agglomerated to generate large magnetic forces. While agglomeration may increase magnetic force upon the concentration of particles (see Section S3.5), our more subtle comparison of magnetic forces versus Stokes drag forces away from the channel centerline is sufficient to correctly predict Xu's results.

### 5.3. Tumor Remission in Yoshida Sarcoma-Bearing Rats by Selective Targeting of Magnetic Albumin Microspheres Containing Doxorubicin [39,92]

Widder *et al.* conducted *in-vivo* experiments on rats to target tumors located on the tail using magnetically responsive microspheres and an external magnet. These microspheres are composed of a coat of albumin surrounding magnetic material (magnetite nanoparticles with 10-20 nm diameters) and a chemotherapy agent (doxorubicin). Magnetic material composition within microspheres has a wide range but is typically between 20% to 50% by weight (w/w) [93]. Knowing the density of the albumin shell (1.36 g/ml [94]), the number of particles within a 1-micron sized microsphere can be approximated ( $\approx 6000$  for 20% w/w). They injected the ventral caudal artery near the rat tail tumors with these magnetically responsive albumin microspheres. The permanent bipolar adjustable gap magnet was positioned around the tumor and held for 30 minutes. For cases in which the magnet was applied, the rats saw decreased tumor size over the length of the experiment. Without a magnet, the rats usually had an increased tumor size and eventually died during the experiment. These data suggests that the magnetic particles were concentrated by the magnet at the tumor location.

Table 2 shows the numbers for this experiment. There is a range of appropriate magnetic-Richardson numbers here, from  $\Psi \approx 0.04$  (for small capillaries) to  $\Psi \approx 2 \times 10^{-5}$  (for major vessels). Likewise, the Péclet number varies from  $4 \times 10^3$  to  $2 \times 10^5$ . Finally, the Renkin diffusion coefficient, determined from Equation (19), ranges between  $\phi \approx 0.05$  when in sinusoidal capillaries (liver, spleen and bone marrow) and essentially zero when in continuous capillaries and fenestrated capillaries. For tumors with leaky vessels that have an average membrane pore size of 600 nm, the maximum Renkin number is  $\phi \approx 0.002$ . Based on this, we predict that the behavior delineation position will be  $\lambda \approx 2.2 \times 10^{-5}$  for capillaries and  $\lambda \approx 2.2 \times 10^{-6}$  in large vessels. Since the delineation position is well to the left of the magnetic-Richardson number, the behavior will primarily be boundary layer formation. We thus predict, except for situations where the Renkin number approaches unity (for damaged or sinusoidal vessels), that the particles can be accumulated to higher concentrations due to a boundary layer formation in the tail for all physiological conditions – for small and large vessels, with fast and slow blood vessel velocities. Since the rat tumors decreased in size due to magnetic forces, it is reasonable to conclude that the magnetic particles were targeted into and around the tumor location. This matches our theoretical predictions above.

### 5.4. Preclinical Trials Experiences with Magnetic Drug Targeting [6,15]

The rat experiments of Figure 1b are used as an example throughout this paper. The non-dimensional numbers for these experiments are summarized in Table 2 under 'Bergemann'. Here, for a 1 mm focusing depth, the magnetic-Richardson number  $\Psi$  varies from 0.14 in capillaries to  $1.5 \times 10^{-4}$  in large vessels and the Péclet number varies similarly from 1000 to  $2 \times 10^5$ . The Renkin reduced diffusion coefficient is effectively zero for continuous and fenestrated capillaries. In sinusoidal capillaries the Renkin value is approximately  $\phi \approx 0.56$  and within leaky vessels with an average pore size of  $\approx 600$  nm the Renkin value is  $\phi \approx$

0.36. From these values, the behavior delineation position is predicted to be  $\lambda \approx 5 \times 10^{-5}$  in capillaries and  $\lambda \approx 2.2 \times 10^{-6}$  in large vessels.

Since  $\Psi$  far exceeds  $\lambda$ , both capillaries and large vessels at  $\leq 1$  mm depth will experience a boundary layer formation behavior, except for situations where the Renkin number closely approaches unity (for damaged vessels) then velocity dominated behavior occurs. Figure 9 shows the predicted transient and equilibrium ferrofluid concentration for a capillary and major blood vessel at 1 mm depth near the magnet. Ferrofluid focusing is seen near the blood vessel wall for both the slowest (capillary) and the fastest (major artery) blood flow.

### 5.5. Clinical Experiences with Magnetic Drug Targeting [7]

Lubbe has performed phase I human clinical trials for the treatment of head, neck and breast cancer shallow (near the skin) tumors (last column in Table 2 under 'Lubbe'). At the surface of the tumor (at a 0.5 cm distance from the magnet) the magnetic-Richardson number varies from 0.025 in capillaries to  $1.3 \times 10^{-4}$  in large vessels and the Péclet number varies similarly from 3500 to  $8.3 \times 10^5$ . The Renkin reduced diffusion coefficient is effectively zero for continuous capillaries. In fenestrated capillaries and sinusoidal capillaries the Renkin value is respectively  $\varpi \approx 0.002$  and  $\varpi \approx 0.8$ . Within leaky vessels with an average pore size of  $\approx 600$  nm the Renkin value is  $\varpi \approx 0.7$ . From these values, the boundary position delineation is predicted to be  $\lambda \approx 2.4 \times 10^{-5}$  in capillaries and  $\lambda \approx 4.4 \times 10^{-7}$  in large vessels.

We find that the magnetic-Richardson number  $\Psi$  is several orders of magnitude larger than the behavior delineation position value  $\lambda$  at the surface of the tumors. Therefore a boundary layer formation behavior is predicted at tumor surfaces. A boundary behavior, however, will still occur at some distance within the tissue as long as the magnetic force upon those deeper particles keeps the magnetic-Richardson number within the boundary layer formation regime. The depth of boundary layer formation can be determined within a given force field for physiological blood velocities (capillaries and large vessels) as shown in Figure 10. Up to a depth of 5 cm and 7.9 cm for large vessels and capillaries respectively, the particles will exhibit a boundary layer behavior. After these cutoff distances, the nano-particles will exhibit a velocity dominated behavior and will be washed away by blood flow in major and minor blood vessels respectively. Between a distance of 5 cm and 7.9 cm, the particles will transition from a complete boundary layer behavior to a velocity dominated behavior getting washed away first in larger vessels that exhibit a higher blood velocity.

During Lubbe's clinical trials, nanoparticles were observed to be targeted approximately within 5 cm [95] of the magnet located at the tumor site by magnetic resonance imaging immediately after treatment (Figure 1a), a finding that is consistent with our predictions here [7]. If the same sized particles with a stronger and larger magnet were used, such as a 2 Tesla (MRI strength) electromagnet with a 25 cm diameter, 20 cm length and 5 cm air core, then we predict that targeting would be possible to a depth of 20 cm in large vessels and to a depth of 30 cm in capillaries.

### 5.6. Summary of Cases

Figure 11 shows a graphical representation of all the experimental cases considered in this paper and compares them to our predicted behavior. For the human clinical trials (Lubbe), the experimental domain is represented more accurately as being curved because the magnetic-Richardson number and the mass Péclet number both vary together across human physiological conditions: blood velocity is higher in bigger blood vessels [1]. This affects both the Richardson and Péclet numbers (see equations (16) and (17)). It was possible to quantify the upper and lower bound curves for human experiments (Lubbe), but not for animal experiments (Widder and Bergemann), because more published physiological data is

available for humans. A detailed analysis and derivation of the curves used is provided in the Supplementary Information (Section S4).

Figure 11 also shows where the magnet creates a concentration in the tissue that is greater than the systemic injected concentration. In the boundary layer domain, even though particles accumulate at the blood/membrane interface, there are some cases where that accumulation is high enough to create a  $C > 1$  in the surrounding tissue, and others where the accumulated amount is insufficient. The cases where more tissue accumulation occurs are influenced by the endothelium thickness to blood vessel diameter ratio, and this additional geometric consideration adds a further non-dimensional number that can be varied. In Figure 11, the lightly shaded regions (light yellow in B, light purple in C, and light pink in D) show the extent of the experimental domains that are predicted to have a tissue concentration greater than unity. Here we assumed a representative endothelium thickness to vessel diameter ratio, a ratio that corresponds to a typical arteriole.

## 6. Conclusion

It is not enough to compare Stokes drag at the centerline to magnetic forces to conclude whether particles can or cannot be magnetically captured against blood flow. Such a comparison dramatically under-predicts the ability of magnetic forces to capture particles because it does not account for the near-zero velocity of blood near vessel walls nor the effects of diffusion. We have carried out a detailed analysis to better understand and quantify the behavior of magnetizable particles *in-vivo*. We find that there are three types of behaviors (velocity dominated, magnetic dominated, and boundary-layer formation) uniquely identified by three essential non-dimensional numbers (the magnetic-Richardson, mass Péclet, and Renkin numbers). Figures 5, 6, 7, and 8 allow magnetic drug delivery researchers to readily determine which behavior should occur in their experiments. These three behaviors remain present even if we consider additional realistic and complicating features, such as blood flow pulsatility, non-uniform magnetic fields, curved blood vessels, and particle agglomeration, although these added effects can modestly shift the delineations between the behaviors. Only the presence of skin, which creates a new interface where particles can build up, adds a qualitatively new behavior and it would require the addition of a fourth non-dimensional number to map out its effect. A comprehensive comparison to prior published *in-vitro* and *in-vivo* experiments shows excellent agreement and explains results that were not previously understood.

## Supplementary Material

Refer to Web version on PubMed Central for supplementary material.

## Works Cited

1. Berne, RM.; Levy, MN. Cardiovascular Physiology. St. Louis, MO: Mosby-Year Book; 1992.
2. Allen, ED.; Burdette, JH. Questions and Answers in MRI. 2nd. 2001.
3. Lemke AJ, von Pilsach MIS, Lubbe A, Bergemann C, Riess H, Felix R. MRI after magnetic drug targeting in patients with advanced solid malignant tumors. European Radiology Nov;2004 14:1949–1955. [PubMed: 15300401]
4. Lubbe AS, Alexiou C, Bergemann C. Clinical applications of magnetic drug targeting. Journal of Surgical Research Feb;2001 95:200–206. [PubMed: 11162046]
5. Lubbe AS, Bergemann C, Brock J, McClure DG. Physiological aspects in magnetic drug-targeting. Journal of Magnetism and Magnetic Materials Apr;1999 194:149–155.

6. Lubbe AS, Bergemann C, Huhnt W, Fricke T, Riess H, Brock JW, Huhn D. Preclinical experiences with magnetic drug targeting: Tolerance and efficacy. *Cancer Research* Oct 15;1996 56:4694–4701. [PubMed: 8840986]
7. Lubbe AS, Bergemann C, Riess H, Schriever F, Reichardt P, Possinger K, Matthias M, Dorken B, Herrmann F, Gurtler R, Hohenberger P, Haas N, Sohr R, Sander B, Lemke AJ, Ohlendorf D, Huhnt W, Huhn D. Clinical experiences with magnetic drug targeting: A phase I study with 4'-epidoxorubicin in 14 patients with advanced solid tumors. *Cancer Research* Oct 15;1996 56:4686–4693. [PubMed: 8840985]
8. Holligan DL, Gillies GT, Dailey JP. Magnetic guidance of ferrofluidic nanoparticles in an in vitro model of intraocular retinal repair. *Nanotechnology* 2003;14:661–666.
9. Arruebo M, Fernández-Pacheco R, Ibarra MR, Santamaría J. Magnetic nanoparticles for drug delivery. *Nano Today* 2007;2
10. Jurgons R, Seliger C, Hilpert A, Trahms L, Odenbach S, Alexiou C. Drug loaded magnetic nanoparticles for cancer therapy. *Journal of Physics-Condensed Matter* Sep 27;2006 18:S2893–S2902.
11. Orekhova NM, Akchurin RS, Belyaev AA, Smirnov MD, Ragimov SE, Orekhov AN. Local prevention of thrombosis in animal arteries by means of magnetic targeting of aspirin-loaded red cells. *Thrombosis research* 1990;57:611. [PubMed: 2326776]
12. Pankhurst QA, Connolly J, Jones SK, Dobson J. Applications of magnetic nanoparticles in biomedicine. *Journal of Physics D: Applied Physics* 2003;R167.
13. Shinkai M. Functional magnetic particles for medical application. *Journal of Bioscience and Bioengineering* 2002;94:606–613. [PubMed: 16233357]
14. Torchilin VP. Drug targeting. *European Journal of Pharmaceutical Sciences* 2000;11:81–91. [PubMed: 10913756]
15. A. Lubbe and C. Bergemann, Email Exchange ed, B. Shapiro, Ed., 2005.
16. Alexiou C, Arnold W, Klein RJ, Parak FG, Hulin P, Bergemann C, Erhardt W, Wagenpfeil S, Lubbe AS. Locoregional Cancer Treatment with Magnetic Drug Targeting 1. 2000;60:6641–6648. AACR.
17. Alexiou C, Jurgons R, Seliger C, Kolb S, Heubeck B, Iro H. Distribution of mitoxantrone after magnetic drug targeting: Fluorescence microscopic investigations on VX2 squamous cell carcinoma cells. *Zeitschrift Fur Physikalische Chemie-International Journal of Research in Physical Chemistry & Chemical Physics* 2006;220:235–240.
18. Simon C. Magnetic drug targeting. New paths for the local concentration of drugs for head and neck cancer. *HNO* Jul;2005 53:600–601. [PubMed: 15868128]
19. Kopke RD, Wassel RA, Mondalek F, Grady B, Chen K, Liu J, Gibson D, Dormer KJ. Magnetic nanoparticles: inner ear targeted molecule delivery and middle ear implant. *Audiol Neurotol* 2006;11:123–133.
20. Shapiro, B.; Rutel, I.; Dormer, K. A System to Inject Therapeutically-coated Magnetic Nanoparticles into the Inner Ear: Design and Initial Validation. *Proceedings of the 3rd International Conference on Micro- and Nanosystems, IDETC 2009; San Diego, CA. 2009.*
21. Alexiou C, Jurgons R, Schmid R, Hilpert A, Bergemann C, Parak F, Iro H. In vitro and in vivo investigations of targeted chemotherapy with magnetic nanoparticles. *Journal of Magnetism and Magnetic Materials* 2005;293:389–393. 2005/5.
22. Barry JW, Bookstein JJ, Alksne JF. Ferromagnetic embolization. Experimental evaluation. *Radiology* February 1;1981 138:341–349. [PubMed: 7455113]
23. Kuznetsov AA, Filippov VI, Alyautdin RN, Torshina NL, Kuznetsov OA. Application of magnetic liposomes for magnetically guided transport of muscle relaxants and anti-cancer photodynamic drugs. *Journal of Magnetism and Magnetic Materials* 2001;225:95–100.
24. Moroz P, Jones SK, Winter J, Gray BN. Targeting liver tumors with hyperthermia: ferromagnetic embolization in a rabbit liver tumor model. *Journal of Surgical Oncology* 2001;78:22–29. [PubMed: 11519064]
25. Okuhata Y. Delivery of diagnostic agents for magnetic resonance imaging. *Advanced Drug Delivery Reviews* 1999;37:121–137. [PubMed: 10837731]

26. Rosengart AJ, Kaminski MD, Chen HT, Caviness PL, Ebner AD, Ritter JA. Magnetizable implants and functionalized magnetic carriers: A novel approach for noninvasive yet targeted drug delivery. *Journal of Magnetism and Magnetic Materials* May 1;2005 293:633–638.
27. Schulze K, Koch A, Schöpf B, Petri A, Steitz B, Chastellain M, Hofmann M, Hofmann H, von Rechenberg B. Intraarticular application of superparamagnetic nanoparticles and their uptake by synovial membrane—an experimental study in sheep. *Journal of Magnetism and Magnetic Materials* 2005;293:419–432.
28. Wilson MW, Kerlan RK Jr, Fidelman NA, Venook AP, LaBerge JM, Koda J, Gordon RL. Hepatocellular Carcinoma: Regional Therapy with a Magnetic Targeted Carrier Bound to Doxorubicin in a Dual MR Imaging/ Conventional Angiography Suite—Initial Experience with Four Patients. *Radiology* January 1;2004 230:287–293. [PubMed: 14695402]
29. Xu H, Song T, Bao X, Hu L. Site-directed research of magnetic nanoparticles in magnetic drug targeting. *Journal of Magnetism and Magnetic Materials* 2005;293:514–519.
30. Decuzzi P, Pasqualini R, Arap W, Ferrari M. Intravascular Delivery of Particulate Systems: Does Geometry Really Matter? *Pharmaceutical Research* 2009;26:235–243. [PubMed: 18712584]
31. Fournier, RL. Basic transport phenomena in biomedical engineering. New York: Taylor & Francis; 2007.
32. Hobbs SK, Monsky WL, Yuan F, Roberts WG, Griffith L, Torchilin VP, Jain RK. Regulation of transport pathways in tumor vessels: Role of tumor type and microenvironment. *PNAS* April 14;1998 95:4607–4612. [PubMed: 9539785]
33. Saltzman, WM. Drug delivery: engineering principles for drug therapy. New York, NY: Oxford University Press; 2001.
34. Rosensweig, RE. Ferrohydrodynamics. Mineola, NY: Dover Publications, Inc.; 1985.
35. Shapiro, B.; Probst, R.; Potts, HE.; Diver, DA.; Lubbe, A. Control to Concentrate Drug-Coated Magnetic Particles to Deep-Tissue Tumors for Targeted Cancer Chemotherapy. 46th IEEE Conference on Decision and Control; New Orleans, LA. 2007. p. 3901-3906.
36. Mikkelsen, CI. Department of Micro and Nanotechnology. Lyngby, Denmark: Technical University of Denmark; 2005. Magnetic separation and hydrodynamic interactions in microfluidic systems.
37. Zimmermann U, Pilwat G. Organ specific application of drugs by means of cellular capsule systems. *Zeitschrift für Naturforschung Section C Biosciences* 1976;31:732–736.
38. Morimoto Y, Okumura M, Sugibayashi K, Kato Y. Biomedical Applications of Magnetic Fluids .2. Preparation and Magnetic Guidance of Magnetic Albumin Microsphere for Site Specific Drug Delivery In vivo. *Journal of Pharmacobio-Dynamics* 1981;4:624–631. [PubMed: 7299625]
39. Widder KJ, Morris RM, Poore G, Howard DP, Senyei AE. Tumor Remission in Yoshida Sarcoma-Bearing Rats by Selective Targeting of Magnetic Albumin Microspheres Containing Doxorubicin. *PNAS* 1981;78:579–581. [PubMed: 6941258]
40. Kato T, Nemoto R, Mori H, Abe R, Unno K, Goto A, Murota H, Harada M, Homma M. Magnetic microcapsules for targeted delivery of anticancer drugs. *Applied Biochemistry and Biotechnology* 1984;10:199–211. [PubMed: 6441520]
41. Gupta PK, Hung CT, Rao NS. Ultrastructural disposition of adriamycin-associated magnetic albumin microspheres in rats. *Journal of Pharmaceutical Sciences* 1989;78:290–294. [PubMed: 2724092]
42. Gupta PK, Hung CT. Effect of carrier dose on the multiple tissue disposition of doxorubicin hydrochloride administered via magnetic albumin microspheres in rats. *Journal of Pharmaceutical Sciences* 1989;78:745–748. [PubMed: 2585268]
43. Gupta PK, Hung CT. Comparative disposition of adriamycin delivered via magnetic albumin microspheres in presence and absence of magnetic field in rats. *Life Sciences* 1990;46:471–479. [PubMed: 2304381]
44. Hafeli UO, Sweeney SM, Beresford BA, Humm JL, Macklis RM. Effective targeting of magnetic radioactive <sup>90</sup>Y-microspheres to tumor cells by an externally applied magnetic field. Preliminary in vitro and in vivo results. *Nuclear Medicine and Biology* 1995;22:147–155. [PubMed: 7767307]

45. Goodwin SC, Bittner CA, Peterson CL, Wong G. Single-Dose Toxicity Study of Hepatic Intra-arterial Infusion of Doxorubicin Coupled to a Novel Magnetically Targeted Drug Carrier. *Toxicol Sci* March 1;2001 60:177–183. [PubMed: 11222884]
46. Engel-Herbert R, Hesjedal T. Calculation of the magnetic stray field of a uniaxial magnetic domain. *Journal of Applied Physics* 2005;97:74504–74505.
47. Hiemenz, PC.; Rajagopalan, R. Principles of Colloid and Surface Chemistry. 3. New York, Basel, Hong Kong: Marcel Dekker, Inc.; 1997.
48. Braun RD, Abbas A, OBukhart SO, Willson W III. Hemodynamic Parameters in Blood Vessels in Choroidal Melanoma Xenografts and Rat Choroid. *Investigative Ophthalmology and Visual Science* 2002;43:3045–3052. [PubMed: 12202528]
49. Fisher AJ, Schrader NW, Klitzman B. Effects of chronic hypoxia on capillary flow and hematocrit in rat skeletal muscle. *American Journal of Physiology- Heart and Circulatory Physiology* 1992;262:1877–1883.
50. Roy JW, Mayrovitz HN. Microvascular blood flow in the normotensive and spontaneously hypertensive rat. *Hypertension, Journal of the American Heart Association* 1982;4:264–271.
51. Ganguly R, Gaind AP, Sen S, Puri IK. Analyzing ferrofluid transport for magnetic drug targeting. *Journal of Magnetism and Magnetic Materials* 2005;289:331–334.
52. Nobuto H, Sugita T, Kubo T, Shimose S, Yasunaga Y, Murakami T, Ochi M. Evaluation of systemic chemotherapy with magnetic liposomal doxorubicin and a dipole external electromagnet. *International Journal of Cancer* 2004;109:627–635.
53. Woodcock JP. Physical properties of blood and their influence on blood-flow measurement. *Reports on Progress in Physics* 1976;39:65–127.
54. Nichols, WW.; O'Rourke, MF. McDonald's Blood Flow in Arteries: Theoretical, Experimental and Clinical Principles. London, UK: Hodder Arnold; 2005.
55. Douglas J. Alternating direction methods for three space variables. *Numerische Mathematik* 1962;4:41–63.
56. Douglas J, Gunn JE. A general formulation of alternating direction methods. *Numerische Mathematik* 1964;6:428–453.
57. Douglas J, Percy CM. On convergence of alternating direction procedures in the presence of singular operators. *Numerische Mathematik* 1963;5:175–184.
58. Peaceman DW, Rachford HH Jr. The numerical solution of parabolic and elliptic differential equations. *Journal of the Society for Industrial and Applied Mathematics* 1955:28–41.
59. Li XL, Yao KL, Liu ZL. CFD study on the magnetic fluid delivering in the vessel in high-gradient magnetic field. *Journal of Magnetism and Magnetic Materials* 2008;320:1753–1758.
60. Yuan F, Dellian M, Fukumura D, Leunig M, Berk DA, Torchilin VP, Jain RK. Vascular Permeability in a Human Tumor Xenograft: Molecular Size Dependence and Cutoff Size. *Cancer Research* 1995;55:3752–3756. [PubMed: 7641188]
61. Alberts, B.; Johnson, A.; Lewis, J.; Raff, M.; Roberts, K.; Walter, P. Molecular biology of the cell. 5th. Garland Science; 2008.
62. Willmott, N.; Daly, JM. Microspheres and regional cancer therapy. Boca Raton, Florida: CRC Press; 1994.
63. Shapiro B. Towards Dynamic Control of Magnetic Fields to Focus Magnetic Carriers to Targets Deep Inside the Body. *Journal of Magnetism and Magnetic Materials* May;2009 321:1549–1599.
64. Shapiro, B.; Probst, R.; Potts, HE.; Diver, DA.; Lubbe, AS. Dynamic Control of Magnetic Fields to Focus Drug-Coated Nano-Particles to Deep Tissue Tumors. 7th International Conference on the Scientific and Clinical Applications of Magnetic Carriers; Vancouver, British Columbia. 2008.
65. Incropera, FP. Fundamentals of heat and mass transfer. Hoboken, NJ: John Wiley; 2007.
66. Bergethon, PR. The physical basis of biochemistry: the foundations of molecular biophysics. Springer; 1998.
67. Fleisch, DA. A student's guide to Maxwell's equations. Cambridge, UK; New York: Cambridge University Press; 2008.
68. Lerner, LS. Physics for scientists and engineers. Jones and Bartlett; 1997.

69. Grief AD, Richardson G. Mathematical modeling of magnetically targeted drug delivery. *Journal of Magnetism and Magnetic Materials - Proceedings of the Fifth International Conference on Scientific and Clinical Applications of Magnetic Carriers* 2005;293:455–463.
70. Feynman, RP.; Leighton, RB.; Sands, M. *The Feynman Lectures on Physics*. Addison-Wesley Publishing Company; 1964.
71. Lide, DR. *Handbook of Chemistry and Physics*. 82. New York: CRC Press LLC; 2001.
72. Schenck JF. The role of magnetic susceptibility in magnetic resonance imaging. *Medical Physics* 1996;23:815–850. [PubMed: 8798169]
73. Vignaud A, Maître X, Guillot G, Durand E, de Rochefort L, Robert P, Vivès V, Santus R, Darrasse L. Magnetic susceptibility matching at the air-tissue interface in rat lung by using a superparamagnetic intravascular contrast agent: Influence on transverse relaxation time of hyperpolarized helium-3. *Magnetic Resonance in Medicine* 2005;54:28–33. [PubMed: 15968677]
74. Forbes ZG, Yellen BB, Barbee KA, Friedman G. An approach to targeted drug delivery based on uniform magnetic fields. *IEEE Transactions on Magnetics Sep*;2003 39:3372–3377.
75. Forbes ZG, Yellen BB, Halverson DS, Fridman G, Barbee KA, Friedman G. Validation of high gradient magnetic field based drug delivery to magnetizable implants under flow. *IEEE Transactions on Biomedical Engineering* 2008;55:643–649. [PubMed: 18270000]
76. Panton, RL. *Incompressible flow*. New York, NY: John Wiley & Sons, INC.; 1984.
77. Sutterby JL. Falling sphere viscometry. I. Wall and inertial corrections to Stokes' law in long tubes. *Journal of Rheology* 1973;17:559.
78. Mendeleev VS, Ivanov AO. Ferrofluid aggregation in chains under the influence of a magnetic field. *Physical Review E* 2004;70:51502.
79. Wu M, Xiong Y, Jia Y, Niu H, Qi H, Ye J, Chen Q. Magnetic field-assisted hydrothermal growth of chain-like nanostructure of magnetite. *Chemical Physics Letters* 2005;401:374–379.
80. Zubarev AY, Odenbach S, Fleischer J. Rheological properties of dense ferrofluids. Effect of chain-like aggregates. *Journal of magnetism and magnetic materials* 2002;252:241–243.
81. Karp, G. *Cell and molecular biology : concepts and experiments*. Chichester: John Wiley; 2008.
82. Anderson JD. *Fundamentals of aerodynamics*. 1984
83. Smith NP, Pullan AJ, Hunter PJ. An anatomically based model of transient coronary blood flow in the heart. *SIAM Journal on Applied mathematics* 2001;990–1018.
84. Hilger I, Hergt R, Kaiser WA. Use of magnetic nanoparticle heating in the treatment of breast cancer. 2005:33–39.
85. Lee CS, Lee H, Westervelt RM. Microelectromagnets for the control of magnetic nanoparticles. *Applied Physics Letters* 2001;79:3308.
86. Tang T, Zheng JW, Chen B, Li H, Li X, Xue KY, Ai X, Zou SQ. Effects of targeting magnetic drug nanoparticles on human cholangiocarcinoma xenografts in nude mice. *Hepatobiliary Pancreat Dist June* 15;2007 6:303–307.
87. Goodwin S, Peterson C, Hoh C, Bittner C. Targeting and retention of magnetic targeted carriers (MTCs) enhancing intra-arterial chemotherapy. *Journal of Magnetism and Magnetic Materials* 1999;194:132–139.
88. Kirk KM, Merte H. A mixed natural/forced convection nucleate boiling heat transfer criteria. 1994:479.
89. Renkin EM. Filtration, diffusion, and molecular sieving through porous cellulose membranes. *Journal of General Physiology* 1954;38:225–243. [PubMed: 13211998]
90. Bruno OP, Lyon M. High-order unconditionally-stable FC-AD PDE solvers for general domains. 2008
91. Beni CE, Bruno OP, Nacev AN, Shapiro B. A fast high-order algorithm enabling efficient solution of a drug-delivery problem. under preparation.
92. Widder KJ, Senyei AE, Ranney DF. Magnetically responsive microspheres and other carriers for the biophysical targeting of antitumor agents. *Advances in pharmacology and chemotherapy* 1979;16:213. [PubMed: 382799]
93. Senyei A, Widder K, Czerlinski G. Magnetic guidance of drug carrying microspheres. *Journal of Applied Physics* 1978;49:3578.

94. Caldwell KD, Karaiskakis G, Myers MN, Calvin Giddings J. Characterization of Albumin Microspheres by Sedimentation Field-Flow Fractionation. *Journal of Pharmaceutical Sciences* 1981;70
95. A. Lubbe, Email Exchange ed, B. Shapiro, Ed., 2008.
96. Comsol, AB. COMSOL multiphysics user's guide. COMSOL AB; Burlington, MA, USA: 2005.
97. Spitz, K.; Moreno, J. A practical guide to groundwater and solute transport modeling. New York: John Wiley; 1996.
98. Young DM. Iterative Solution of Large Linear Systems. Dover. 2003
99. Bruno OP, Han Y, Pohlman MM. Accurate, high-order representation of complex three-dimensional surfaces via Fourier continuation analysis. *Journal of Computational Physics* 2007;227:1094–1125.
100. Holdsworth DW, Norley CJD, Frayne R, Steinman DA, Rutt BK. Characterization of common carotid artery blood-flow waveforms in normal human subjects. *Physiological Measurement* 1999;20:219–240. [PubMed: 10475577]
101. Kirpalani A, Park H, Butany J, Johnston KW, Ojha M. Velocity and wall shear stress patterns in the human right coronary artery. *Journal of biomechanical engineering* 1999;121:370. [PubMed: 10464690]
102. Ku DN. Blood flow in arteries. *Annual Review of Fluid Mechanics* 1997;29:399–434.
103. Myers JG, Moore JA, Ojha M, Johnston KW, Ethier CR. Factors influencing blood flow patterns in the human right coronary artery. *Annals of Biomedical Engineering* 2001;29:109–120. [PubMed: 11284665]
104. Ganguly R, Zellmer B, Puri IK. Field-induced self-assembled ferrofluid aggregation in pulsatile flow. *Physics of Fluids* 2005;17:097104, 1–8.



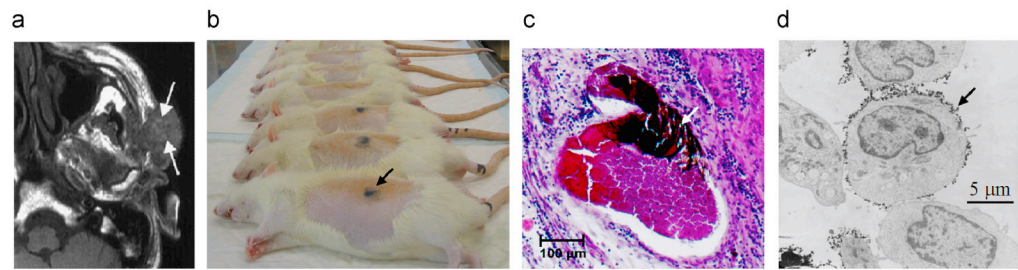


**Figure 1.**

Verification of magnetic drug delivery from the body to the cellular scale in animal and human clinical trials. a) Magnetic resonance (MR) image for a cancer patient, magnetic nano-particle (ferrofluid) accumulation can be seen as lighter regions at the arrow tips (due to the MR extinction phenomena [2]) [3-7]. b) Rat studies: concentrated ferrofluid is visible under the skin [6,15]. c) Ferrofluid concentrated in rabbit tumor micro-vessels (white arrow) [16,17]. d) Magnetic nano-particles at the membrane of mouse epithelial cells (e.g. black arrow) [18].

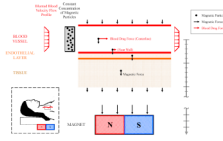


**Figure 2.**

The simulated blood vessel geometry. The blood vessel is idealized as a straight channel. Blood and a constant concentration of magnetic nano-particles enter from the left. The magnetic particles (black circles) within the blood vessel experience diffusion, migration under blood flow, and magnetic forces. Magnetic particles in the surrounding endothelial and tissue layer experience diffusion and magnetic drift but no blood flow forces. The magnet can be a long distance from the blood vessel (deep targeting) and here this is denoted by the break in the length bar on the right of the figure. Inset: The simulated domain around a blood vessel in deep tissue.

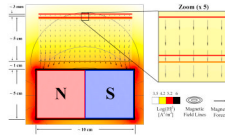


**Figure 3.** Magnetic *forces* are usually constant within the tissue-vessel system. Here even though a magnet is held close to the blood vessel (at a distance that is less than its length) the resulting magnetic force within the blood vessel is still essentially constant: the maximum error of  $|F_{\text{const}} - F_{\text{exact}}| / |F_{\text{exact}}| < 10\%$ .

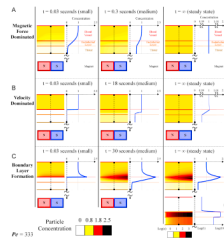


**Figure 4.**

The three prototypical behaviors: A) magnetic force dominated case ( $\Psi = 10^{-3}$ ,  $\varnothing = 1$ ), B) velocity dominated case ( $\Psi = 10^{-5}$ ,  $\varnothing = 10^{-3}$ ), and C) boundary layer formation ( $\Psi = 10^{-2}$ ,  $\varnothing = 10^{-3}$ ). (A) The magnetic force dominated case shows a cross-sectional concentration of the magnetic nano-particles for three times at  $t = 0.03$  seconds (early), 0.3 seconds (middle), and at equilibrium, at  $Pe = 333$ . Particles are pulled towards the magnet and out through the bottom of the tissue resulting in a constant concentration equal to the blood inlet concentration. Here the tissue diffusion is set to equal the diffusion in the endothelial membrane. (B) Velocity dominated shows a cross-sectional concentration of the magnetic nano-particles for three times at  $t = 0.03$  seconds (early), 18 seconds (middle), and at equilibrium, at  $Pe = 333$ . Particles are washed out before they generate a significant boundary layer along the vessel wall. At long times diffusion equilibrates the concentration between tissue and blood. Here the tissue Renkin number is set at  $\varnothing_r = 10 \varnothing$  which means it is ten times as easy for particles to diffuse through tissue than through the endothelial membrane. (C) Boundary layer formation shows a cross-sectional magnetic nano-particle concentration for three times at  $t = 0.03$  seconds (early), 30 seconds (middle), and at equilibrium, at  $Pe = 333$ . (i) The steady state profile for  $\Psi = 10^{-2}$ . Here the particle concentration is shown on the same linear scale as in other time snapshots. (ii) The steady state profile for a higher magnetic-Richardson number, for  $\Psi = 10^{-1}$ . Here both the particle concentration and the cross-sectional plot are shown on a log scale. In both boundary layer cases ( $\Psi = 10^{-2}$  and  $10^{-1}$ ) the particles build-up along the vessel membrane on both the vessel side and within the membrane. The boundary layer forms very rapidly. In (ii) the membrane particle concentration is sufficiently high to cause a concentration in the tissue greater than the vessel inlet concentration. In both (i) and (ii) the tissue Renkin number is set at  $\varnothing_r = 10 \varnothing$  which means it is ten times as easy for particles to diffuse through tissue than through the endothelial membrane.

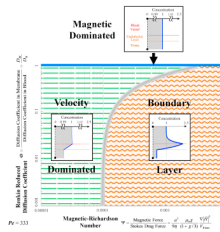


**Figure 5.**

Magnetic nano-particle behaviors as a function of the magnetic-Richardson and Renkin reduced diffusion coefficient non-dimensional numbers. The mass Péclet number was held constant. Three regions are shown: the magnetic dominated region at the top (the thin solid blue region); the velocity (Stokes drag) dominated region on the left (dashed lines region); and the boundary layer formation region on the right (wavy lines region). Notice that boundary layer build-up behavior is still possible even if the magnetic force is just 0.01% of the Stokes drag force at the vessel centerline, i.e. at  $\Psi \geq 0.0001$ . The boundary between the velocity and boundary layer build-up regions is diffuse as shown schematically by the thickness of the fuzzy gray line separating them.

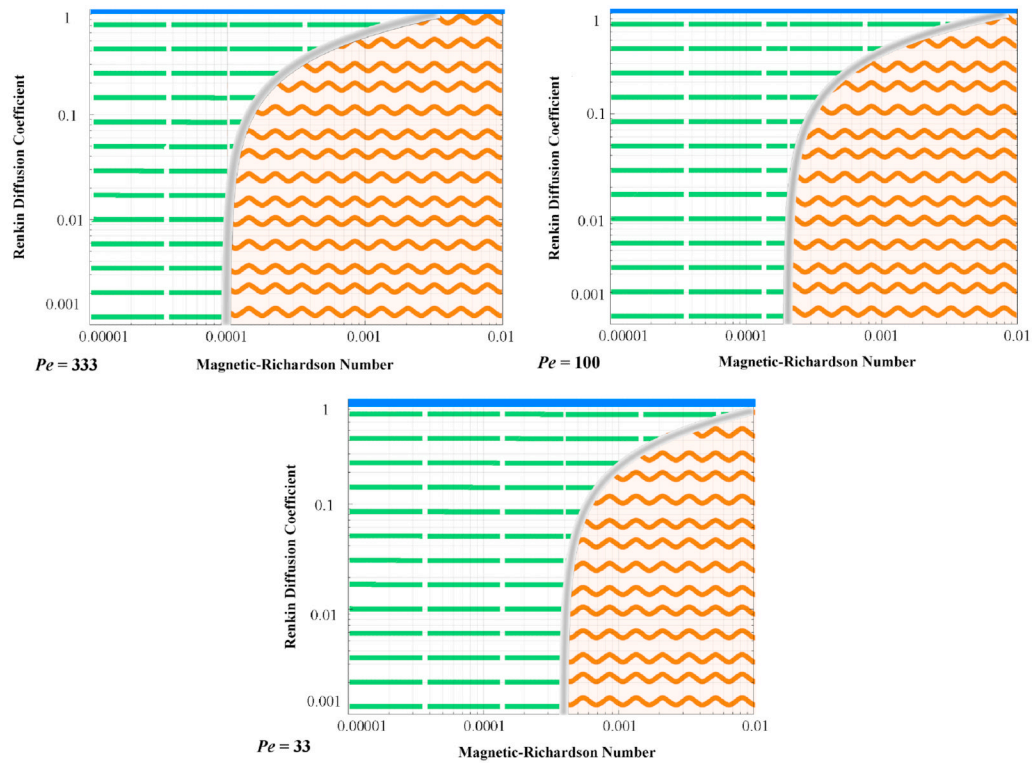


**Figure 6.** Behavioral dependence upon mass Péclet number. As the mass Péclet number decreases, the delineation between behavior types shifts to the right (to larger magnetic-Richardson numbers). In addition, at lower mass Péclet numbers, the magnetic dominated region increases in size towards lower Renkin reduced diffusion coefficients.

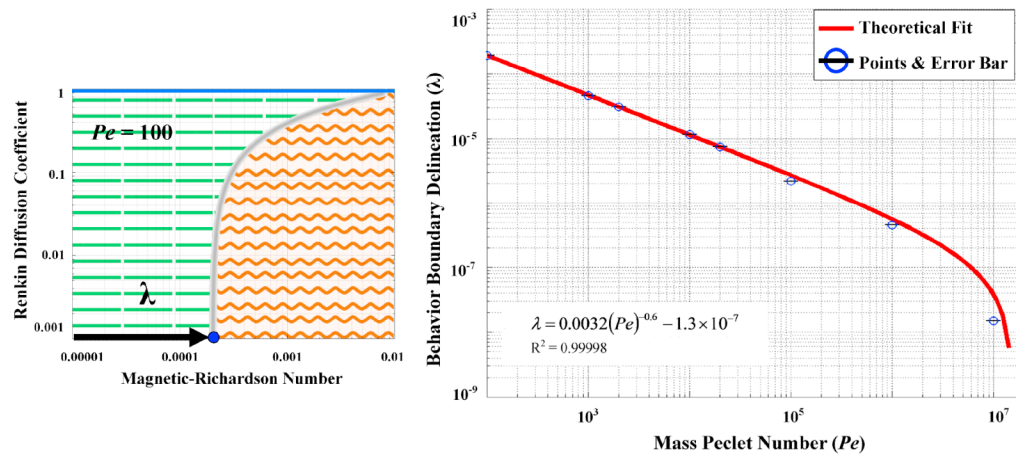


**Figure 7.**

The delineation of the boundary between the velocity dominated and boundary layer formation regimes is denoted by  $\lambda$  (left panel, it is measured along the magnetic-Richardson axis at a Renkin coefficient of  $10^{-3}$ ) and it depends on the mass Péclet number (right panel). The stated equation provides a convenient fit of  $\lambda$  versus  $Pe$  for the curve shown in red.

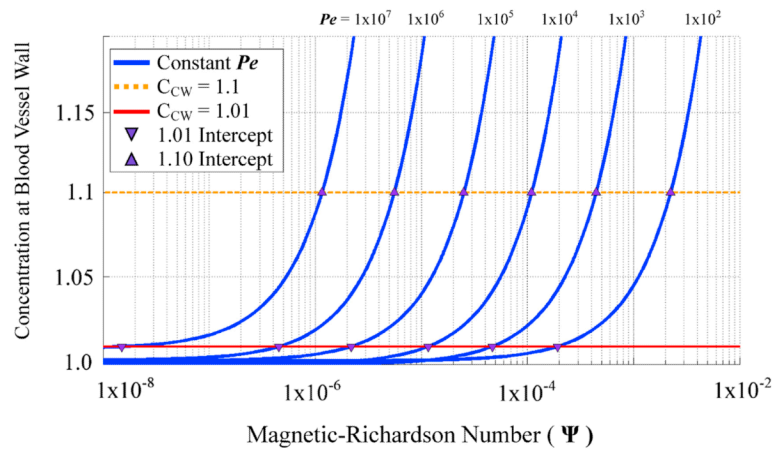


**Figure 8.**

Concentration at the blood vessel wall ( $C_{B,vessel-wall}$ ) versus magnetic-Richardson number for a given mass Péclet number. Curves associated with each constant mass Péclet number are shown in blue. The red line illustrates a concentration cutoff requirement of  $> +1\%$  for boundary build-up behavior. Any magnetic-Richardson number larger than the intercept between the red line and blue curve for a given Péclet number (shown by a downwards purple triangle) will exhibit a boundary build-up behavior. The dotted orange line shows cutoffs for a higher vessel wall concentration requirement of  $> +10\%$ .



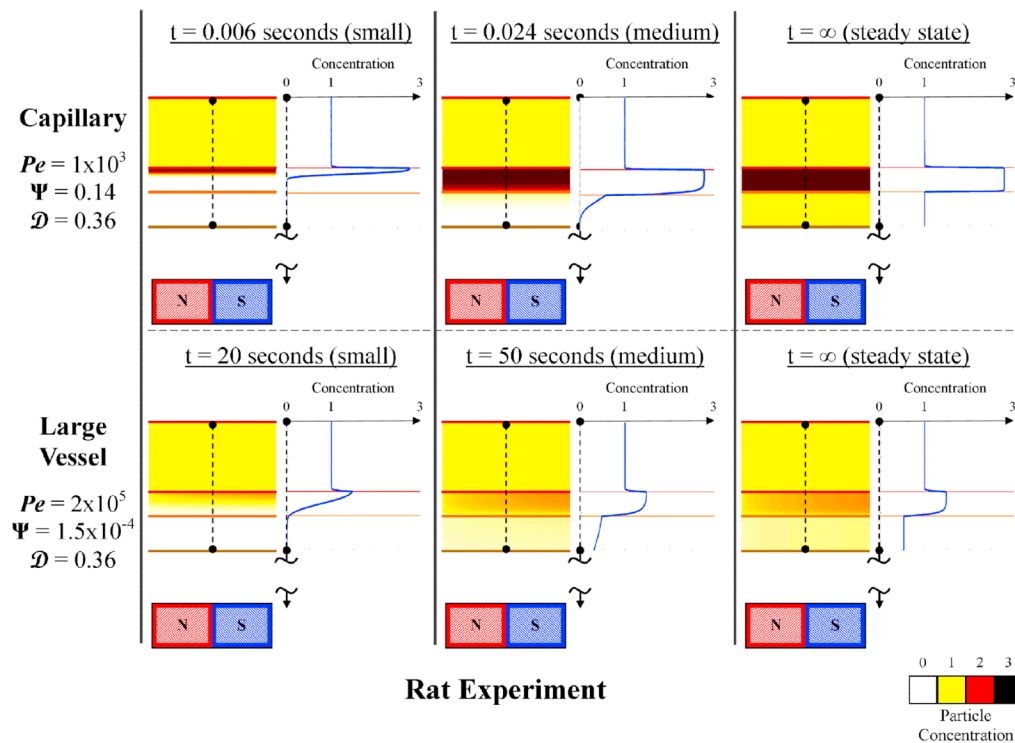


**Figure 9.** Predicted ferrofluid concentrations for 1 mm deep magnetic targeting in the rat experiments of Figure 1b. An initial, intermediate, and final (steady-state) time are shown for capillary (slowest blood flow,  $V_{B \max} = 0.1$  mm/s) and a major blood vessel (fastest blood flow,  $V_{B \max} = 20$  cm/s). Contrary to the crude estimate in the introduction, magnetic focusing is predicted even in the major blood vessels.

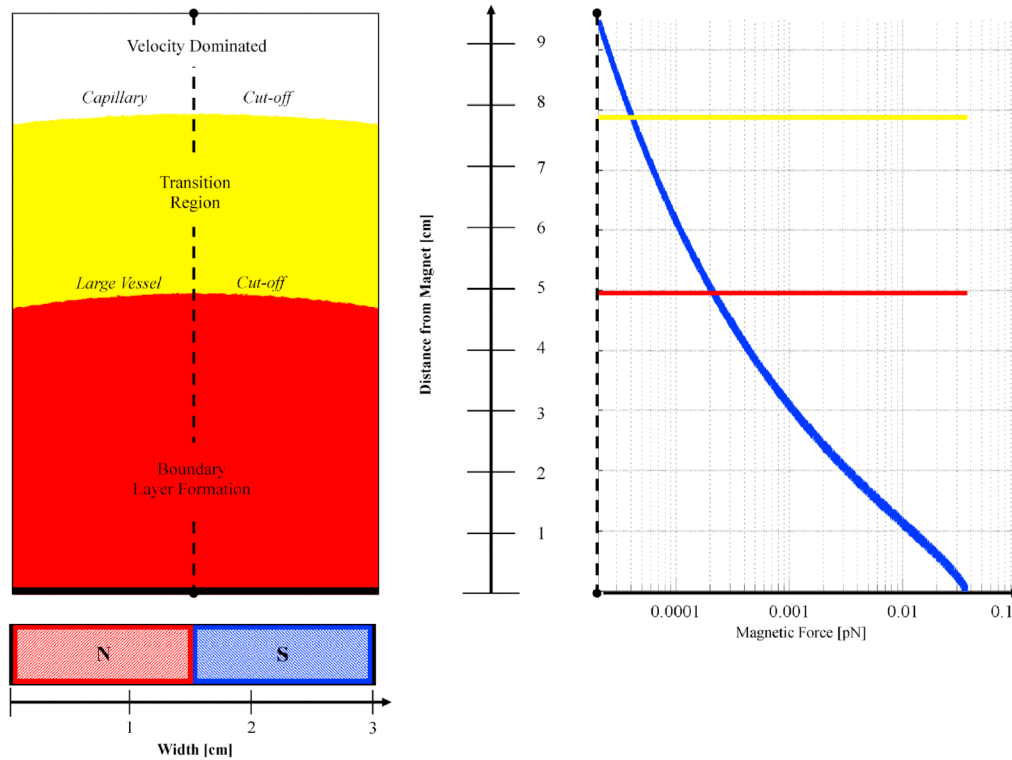


**Figure 10.**

Focusing depth for the Lubbe 0.8 Tesla human clinical trials experiments. The magnet is positioned a distance of 0.5 cm from the skin. The predicted depth of the boundary layer formation, transition, and velocity dominated regions is shown. For particles deeper inside the body, the magnet is unable to exert a sufficient magnetic force (shown on the right) to generate a ferrofluid boundary layer behavior. Focusing of magnetic nano-particles is predicted to be possible in major vessels up to a 5 cm depth, and in capillaries to a greater 7.9 cm depth.

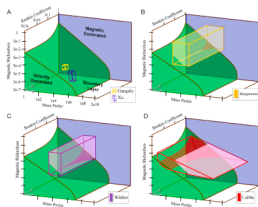


**Figure 11.**

Summary of experimental studies. The firmly shaded regions in green and blue denote the magnetic and velocity behavior domains. The boxed or curved boxed regions show the values spanned by each experiment. The dark shading (dark yellow in B, purple in C, and dark red in D) shows the region of the corresponding experiment that exists in the velocity dominated region. The light shading (light yellow in B, light purple in C, and pink in D) shows the region of the experiments where the concentration created in the tissue is greater than the vessel inlet concentration. The *in-vitro* experiments (A) exist entirely in the boundary layer regime. Widder (B) and Bergemann (C) have small portions in the velocity dominated region, only at small magnetic-Richardson numbers and high Renkin coefficients. Lubbe (D) extends into the velocity behavior domain when mass Péclet numbers and magnetic-Richardson numbers are small, and this extent increases as the Renkin coefficient increases.

**Table 1**

Human physical parameters encountered in magnetic drug delivery. (Essential quantities needed for the subsequent non-dimensionalization are bolded.)

| Parameter                                      | Symbol                        | Parameter Range  |
|--|-------------------------------|--|
| Particle Radius                                | $a$                           | 1 nm – 5 $\mu$ m   |
| Distance from Magnet                           | $d$                           | 1 mm – 30 cm   |
| Magnetic Field Strength(or Magnetic Intensity) | $\frac{ \vec{B} }{ \vec{H} }$ | 0.1 – 1.5 T<br>$8 \times 10^4 - 1.2 \times 10^6$ A/m                                       |
| Magnet Length                                  | $L_M$                         | 1 - 30 cm  |
| Magnetic Drift Velocity                        | $ \vec{V}_R $                 | $9 \times 10^{-15}$ m/s – $3.8 \times 10^{-4}$ m/s   |
| <b>Magnetic Force on a Particle</b>            | $ \vec{F}_M $                 | <b><math>5 \times 10^{-25} - 1.1 \times 10^{-11}</math> N</b>                              |
| <b>Maximum Centerline Blood Velocity</b>       | $V_{B \max}$                  | <b>0.5 mm/s – 40 cm/s</b>  |
| <b>Vessel Diameter</b>                         | $d_B$                         | <b>7 <math>\mu</math>m – 3 cm</b>  |
| Blood Viscosity                                | $\eta$                        | 0.003 Pa s   |
| <b>Centerline Stokes Drag on a Particle</b>    | $ \vec{F}_S $                 | <b><math>3 \times 10^{-14} - 1.1 \times 10^{-7}</math> N</b>                               |
| Temperature                                    | $T$                           | 310 K (body temperature)   |
| Brownian Diffusion Coefficient                 | $D_B$                         | $1 \times 10^{-14} - 1 \times 10^{-12}$ m <sup>2</sup> /s                                  |
| Scattering Diffusion Coefficient               | $D_S$                         | $3.5 \times 10^{-12} - 6 \times 10^{-10}$ m <sup>2</sup> /s                                |
| <b>Total Diffusion Coefficient (in blood)</b>  | $D_{Tot}$                     | <b><math>1 \times 10^{-14} - 6 \times 10^{-10}</math> m<sup>2</sup>/s</b>                  |
| <b>Diffusion Coefficient (in membrane)</b>     | $D_M$                         | <b>0 (if particles larger than pores) - <math>1.5 \times 10^{-12}</math></b>               |
| <b>Diffusion Coefficient (in tissue)</b>       | $D_T$                         | <b>0 (if particles larger than interstitial spaces) - <math>1.2 \times 10^{-14}</math></b> |

Table 2

Parameters for experimental studies reviewed in Sections 5.1 to 5.4. Bolded items are quantities used to determine our three characteristic non-dimensional numbers. Here 'cplry' and 'MG' are used to denote capillary and major blood vessel properties respectively. 'N/A' denotes unapplicable variables because the experiments were completed within glass tubes. '-' denotes unknown variables that are not needed because the magnetic forces were either supplied or could be otherwise be calculated.

| Parameter                | Ganguly                        | Xu                                      | Widder                                  | Bergemann                               | Lubbe                                   |
|--------------------------|--------------------------------|---|---|---|---|
| Particle Radius          | 5 mm                           | 10 mm                                   | 7 nm <sup>a</sup>   0.5 μm <sup>b</sup> | 125 nm                                  | 50 nm                                   |
| Distance to Magnet       | 1 mm                           | --                                      | 5 mm                                    | 1 mm                                    | 0.5 cm                                  |
| Field Strength           | 1.3 T                          | --                                      | 0.55 T                                  | 0.5 T                                   | 0.8 T                                   |
| Magnetic Intensity       | 1 × 10 <sup>6</sup> A/m        | --                                      | 4.3 × 10 <sup>5</sup> A/m               | 3.9 × 10 <sup>5</sup> A/m               | 6.3 × 10 <sup>5</sup> A/m               |
| Magnet Length            | 6 cm                           | --                                      | --                                      | 5 cm                                    | 3 cm                                    |
| <b>Magnetic Force</b>    | <b>4 × 10<sup>-5</sup> pN</b>  | <b>2.6 × 10<sup>-5</sup> pN</b>         | <b>0.12 pN</b>                          | <b>0.1 pN</b>                           | <b>3.5 × 10<sup>-2</sup> pN</b>         |
| Maximum Blood Velocity   | cplry<br>4.8 mm/s              | 5.3 mm/s <sup>*</sup>                   | ≈ 0.1 mm/s                              | ≈ 0.1 mm/s                              | ≈ 0.5 mm/s                              |
|                          | MG                             | 100 mm/s <sup>**</sup>                  | ≈ 20 cm/s                               | ≈ 20 cm/s                               | ≈ 10 cm/s <sup>#</sup>                  |
| Vessel Diameter          | cplry<br>10 mm (3mm effective) | 2 mm                                    | ≈ 6 μm                                  | ≈ 6 μm                                  | ≈ 7 μm                                  |
|                          | MG                             |   | ≈ 1 mm                                  | ≈ 1 mm                                  | ≈ 5 mm                                  |
| Fluid Viscosity          | η                              | 0.001 Pa s                              | 0.003 Pa s                              | 0.003 Pa s                              | 0.003 Pa s                              |
| <b>Stokes Drag Force</b> | cplry<br> F <sub>S</sub>       | <b>1 pN<sup>*</sup></b>                 | <b>3 pN</b>                             | <b>0.7 pN</b>                           | <b>1.4 pN</b>                           |
|                          | MG                             | <b>20 pN<sup>**</sup></b>               | <b>6 nN</b>                             | <b>1.4 nN</b>                           | <b>0.28 nN</b>                          |
| Blood Diff. Coeff.       | D <sub>B</sub>                 | 4 × 10 <sup>-11</sup> m <sup>2</sup> /s | 1 × 10 <sup>-13</sup> m <sup>2</sup> /s | 6 × 10 <sup>-13</sup> m <sup>2</sup> /s | 1 × 10 <sup>-12</sup> m <sup>2</sup> /s |
| Scattering Diff. Coef.   | D <sub>S</sub>                 | Cplry<br>N/A                            | 0                                       | 0                                       | 0                                       |
|                          | MG                             |   | 1 × 10 <sup>-9</sup> m <sup>2</sup> /s  | 1 × 10 <sup>-9</sup> m <sup>2</sup> /s  | 6 × 10 <sup>-10</sup> m <sup>2</sup> /s |
| Membrane Diff. Coef.     | D <sub>M</sub>                 | Small<br>N/A                            | 0                                       | 0                                       | 0                                       |

| Parameter                            | Ganguly | Xu                                       | Widder                                   | Bergemann                                | Lubbe                                    |
|--------------------------------------|---------|--|--|--|--|
|                                      | Large   |  | $1 \times 10^{-13} \text{ m}^2/\text{s}$ | $6 \times 10^{-13} \text{ m}^2/\text{s}$ | $6 \times 10^{-13} \text{ m}^2/\text{s}$ |
| Tissue Diff. Coef.                   | Small   | N/A                                      | 0  | 0  | 0  |
|                                      | Large   |  | $1 \times 10^{-13} \text{ m}^2/\text{s}$ | $6 \times 10^{-13} \text{ m}^2/\text{s}$ | $6 \times 10^{-13} \text{ m}^2/\text{s}$ |
| Diffusion Coefficient                | cply    |  | $1 \times 10^{-13} \text{ m}^2/\text{s}$ | $6 \times 10^{-13} \text{ m}^2/\text{s}$ | $1 \times 10^{-12} \text{ m}^2/\text{s}$ |
|                                      | MG      | $2 \times 10^{-11} \text{ m}^2/\text{s}$ | $1 \times 10^{-9} \text{ m}^2/\text{s}$  | $1 \times 10^{-9} \text{ m}^2/\text{s}$  | $6 \times 10^{-10} \text{ m}^2/\text{s}$ |
| Magnetic-Richardson Number           | cply    |  | $0.04$                                   | $0.14$                                   | $0.025$                                  |
|                                      | MG      | $9 \times 10^{-5}$                       | $2 \times 10^{-5}$                       | $1.5 \times 10^{-4}$                     | $1.3 \times 10^{-4}$                     |
| Mass Péclet Number                   | cply    |  | $4 \times 10^3$                          | $1 \times 10^3$                          | $3.5 \times 10^3$                        |
|                                      | MG      | $3.6 \times 10^5$                        | $2 \times 10^5$                          | $2 \times 10^5$                          | $8.3 \times 10^5$                        |
| Renkin Reduced Diffusion Coefficient | Small   |  | $\approx 0$                              | $\approx 0$                              | $\approx 0$                              |
|                                      | Large   | N/A                                      | $\approx 0.05$                           | $\approx 0.56$                           | $\approx 0.8$                            |
| Behavior Boundary Position           | cply    |  | $2.2 \times 10^{-5}$                     | $5 \times 10^{-5}$                       | $2.4 \times 10^{-5}$                     |
|                                      | MG      | $1.6 \times 10^{-6}$                     | $2.2 \times 10^{-6}$                     | $2.2 \times 10^{-6}$                     | $4.4 \times 10^{-7}$                     |

\* 100% retention of particles;

\*\* 15% retention of particles;

# ignores vena cava and aorta velocities;

$a$  radius of magnetite particle;

$b$  radius of microsphere or liposome